

Dear Topic Editor and Referees,

We are sincerely grateful to receive the valuable comments and suggestions from the reviewers, which are essential for improving the quality of this paper and making our methodology and conclusions more robust. We also appreciate the opportunity to revise the manuscript. Based on the reviewers' suggestions, we have comprehensively revised the text to clarify our methodological framework and strengthen the discussion.

Specifically, we have rewritten Section 2.2 to explicitly articulate the multi-source ensemble framework used to construct the Multi-ensemble Biomass-burning Emissions Inventory (MBEI). This includes clarifying the mechanism for handling temporal resolution by detailing how static inputs are synthesized with dynamic proxies (e.g., NPP and FRP) to reconstruct continuous emission timelines. Furthermore, we refined the description of our uncertainty quantification, explaining how the ensemble of eight independent sub-inventories is used to define the uncertainty range (Mean, Standard Deviation, Maximum, and Minimum), and we have integrated these pixel-scale ensemble statistics into the dataset to explicitly quantify uncertainty.

In addition to these methodological clarifications, we significantly expanded the discussion to address the trade-offs between temporal consistency (MODIS) and spatial resolution (VIIRS), as well as physical limitations regarding small-fire detection and fuel load estimation. We have also condensed the abstract and updated Figure 1 and Table 2 to visually support these changes. We have carefully studied all comments and did our best to revise the manuscript accordingly. The revised parts have been highlighted in yellow, and the detailed point-by-point responses are attached below. The dataset is publicly available at <https://doi.org/10.5281/zenodo.18104830>.

We hope that our responses and revisions are satisfactory.

Yours sincerely,

Shuai Yin

Affiliation: State Key Laboratory of Remote Sensing and Digital Earth, Aerospace Information Research Institute, Chinese Academy of Sciences. Beijing 100101, China

Email: yinshuai@aircas.ac.cn

Responds to the reviewer's comments:

Reviewer #1:

This study presents a new framework (MBEI) that integrates top-down and bottom-up algorithms by combining two fire-detection products with four sets of key input variables, yielding eight distinct sub-inventories of biomass-burning emissions. Compared to existing inventories, these new datasets uniquely provide the maximum–minimum range of all eight sub-inventories, thereby quantifying estimation uncertainty. This rich information allows data users to directly incorporate sensitivity analyses into their own studies and thus provides critical support for exploring complex global biomass-burning dynamics. The paper is well written and offers new insight into biomass-burning research. However, a few points need to be addressed. Therefore, I recommend that the manuscript be accepted for publication after a revision.

Major concerns:

1. Although the new dataset includes eight groups of sub-inventories, the mean values and uncertainty information (e.g., standard deviation, minimum, and maximum) for these ensemble inventories are not provided at the pixel scale. I suggest that the authors calculate these statistics on a per-pixel basis and include them in the dataset. This information is highly valuable to data users and should be made publicly available.

Response: We sincerely thank the reviewer for this highly constructive suggestion regarding the accessibility of pixel-scale uncertainty information. We fully acknowledge that while the generation of eight independent sub-inventories constitutes the structural core of our ensemble framework, the practical utility of this dataset for downstream applications—such as atmospheric transport modeling and air quality assessment—relies heavily on the availability of synthesized statistical metrics at the grid scale. Providing the raw sub-inventories alone places an unnecessary computational burden on the user, whereas pre-calculated ensemble statistics provide immediate, actionable insight into the spatial reliability and variance of the emission estimates.

In direct response to this recommendation, we have rigorously post-processed the ensemble outputs to include pixel-level statistics for the entire study period (2003–2023). Specifically, for every 0.1°

× 0.1° grid cell and for each month, we have calculated the ensemble mean to serve as the central estimate, along with the standard deviation to represent algorithmic dispersion, and the maximum and minimum values to define the full uncertainty range. These four statistical layers have been integrated into the updated MBEI dataset structure and are now publicly accessible via the repository link provided in the Data Availability section. This enhancement ensures that users can seamlessly incorporate both the central emission estimates and their associated uncertainty bounds into their analyses without needing to reconstruct the ensemble statistics manually.

Correspondingly, we have revised the manuscript to formally document this major improvement in data provision. As detailed in the updated introduction of Section 2.2, the description of the MBEI framework has been refined to explicitly state that the final dataset output includes these pixel-level ensemble statistics. We emphasize in the revised text that rather than obscuring differences through data fusion, the MBEI leverages the ensemble spread to define the uncertainty bounds, specifically providing "the ensemble mean as the central estimate, while delineating the uncertainty envelope through two metrics: the standard deviation, representing dispersion, and the maximum and minimum bounds, defining the uncertainty range." Furthermore, we have updated Table 2 to list these statistical metrics as integral components of the final dataset, and the workflow illustrated in Figure 1 has been modified to visually depict the aggregation of the eight sub-inventories into these final statistical layers.

Please refer to Page 10, Lines 243-252 and the following is the revised manuscript:

To quantify global biomass burning emissions and their associated uncertainties, we constructed the MBEI using a multi-source ensemble framework. Unlike conventional approaches that rely on a single algorithm, this framework operates by generating an ensemble of eight independent sub-inventories (see Table 2). This design is explicitly structured to capture the structural uncertainty stemming from the fundamental mechanistic discrepancies between bottom-up (burned area-based) and top-down (fire radiative power-based) methodologies. Rather than obscuring these differences through data fusion, the MBEI leverages them to define the uncertainty bounds of the estimates. Consequently, for each 0.1° grid cell, we provide the ensemble mean as the central estimate, while delineating the uncertainty envelope through two metrics: the standard deviation, representing dispersion, and the maximum and minimum bounds, defining the uncertainty range. The overall

workflow is illustrated in Fig. 1.

Please refer to Fig. 1 and Table 2:

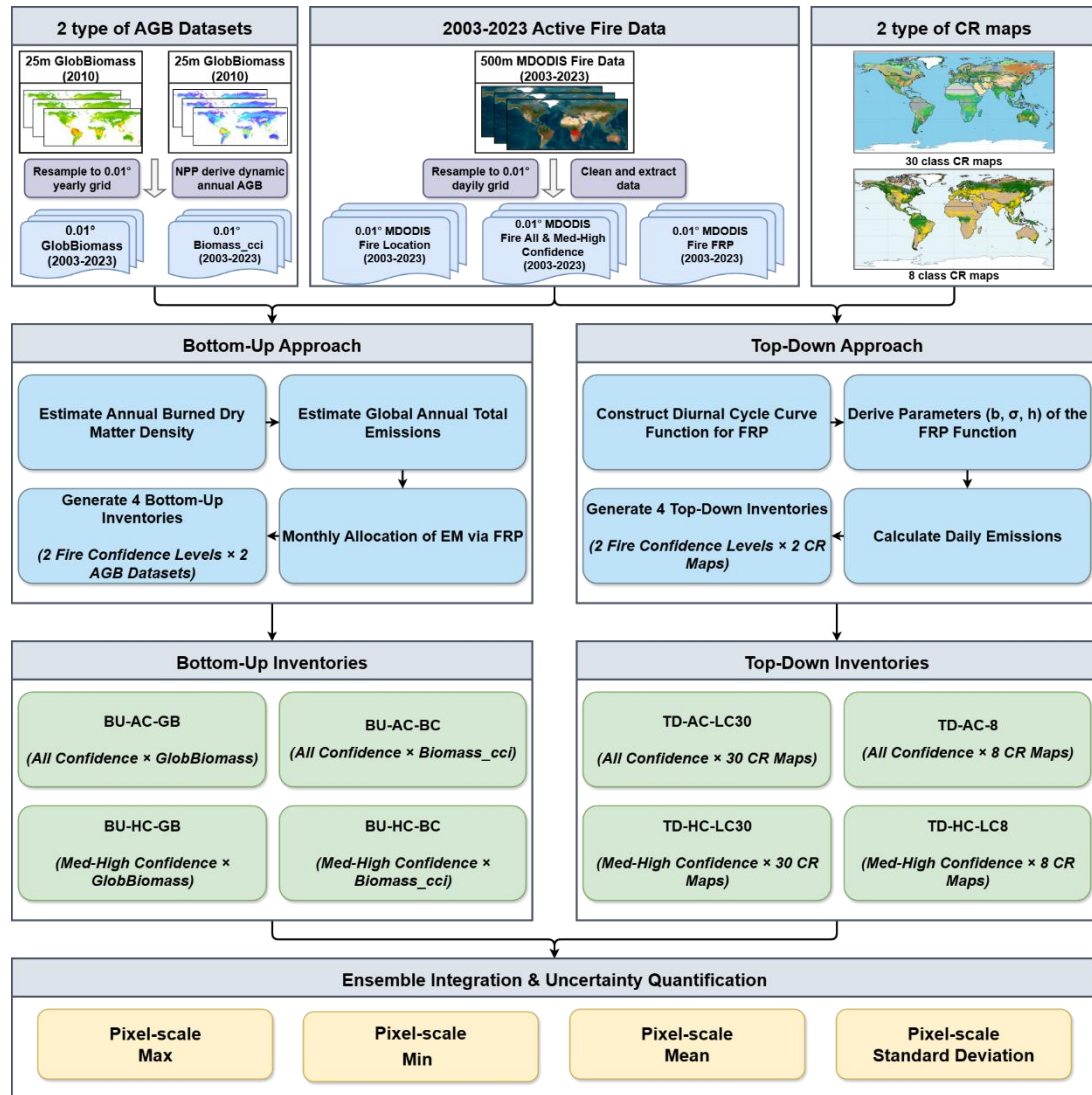


Figure 1. Framework for the construction of MBEL.

Table 2. The detail of the eight biomass burning emission sub-inventories.

4 Bottom-Up Inventories			4 Top-Down Inventories		
Name	Confidence Level	Datasets	Name	Confidence Level	Datasets
BU-AC-GB	All Confidence	GlobBiomass	TD-AC-LC30	All Confidence	30-class CR map
BU-AC-BC	All Confidence	Biomass_cci	TD-AC-LC8	All Confidence	8-class CR map
BU-HC-GB	Medium-to-High confidence	GlobBiomass	TD-HC-LC30	Medium-to-High confidence	30-class CR map
BU-HC-BC	Medium-to-High confidence	Biomass_cci	TD-HC-LC8	Medium-to-High confidence	8-class CR map

Note: The final MBEI dataset also includes the pixel-level ensemble statistics (Mean, Std, Max, Min) calculated from these eight sub-inventories.

2. In this study, only MODIS fire products are used, while the higher-resolution VIIRS is not considered. As the successor to MODIS, VIIRS offers enhanced spatial resolution (375–750 m) and advanced day-night imaging capabilities for superior global monitoring of land, ocean, and atmospheric phenomena. The authors should explicitly state the reason for not including VIIRS observations in the manuscript.

Response: We sincerely appreciate the reviewer’s insight regarding the superior technical capabilities of the VIIRS sensor and the potential benefits of its inclusion. We fully agree with the reviewer’s assessment that VIIRS, serving as the designated successor to MODIS, offers significantly enhanced spatial resolution (375 m versus 1 km) and advanced day-night band capabilities, which are undoubtedly critical for improving the detection of small-scale thermal anomalies that MODIS might overlook. However, the decision to rely exclusively on MODIS active fire products (MCD14DL) for this specific study was driven by the overriding necessity to maintain rigorous temporal homogeneity across the entire 21-year study period (2003–2023).

The primary scientific objective of the MBEI is to analyze long-term trends and interannual variability in global biomass burning. Since the VIIRS record (via Suomi-NPP) only commences in 2012, integrating these data would necessitate splicing a higher-sensitivity sensor into the latter half

of the time series. We argue that mixing the 1-km MODIS record (pre-2012) with the 375-m VIIRS record (post-2012) would introduce significant systematic inconsistencies. Specifically, the superior detection sensitivity of VIIRS would inevitably result in a distinct step-change increase in detected fire counts and radiant energy immediately following its introduction. Such an artificial discontinuity, arising solely from the change in instrumentation, could be easily misinterpreted as a climatological intensification of global fire activity, thereby compromising the validity of the trend analysis that is central to this research. Consequently, to avoid introducing artificial discontinuities into the time series, we prioritized the temporal consistency of the single-sensor MODIS record over the higher spatial resolution offered by VIIRS.

We have explicitly clarified this rationale in Section 4.2 of the revised manuscript to address the reviewer's concern. In this revised discussion, we openly acknowledge the trade-offs inherent in this decision; while prioritizing temporal consistency allows for robust trend detection, it likely results in conservative emission estimates in regions dominated by small, fragmented fires, such as agricultural residues in India or the Middle East. Furthermore, looking ahead, we recognize the immense potential of VIIRS as its data record lengthens. As the VIIRS time series matures into a sufficient multi-decadal record, we plan to apply the MBEI framework to generate a dedicated, high-resolution VIIRS-based emission dataset, thereby fully leveraging its advanced detection capabilities for future monitoring.

Please refer to Page 29, Lines 643-652 and the following is the revised manuscript:

A key decision in this study was to use MODIS active fire products (MCD14DL) exclusively for the 2003–2023 period. Although the Visible Infrared Imaging Radiometer Suite (VIIRS), available since 2012, offers superior spatial resolution (375 m) compared to MODIS (1 km), applying it would have limited the consistent time series to the post-2012 era. Merging MODIS (2003–2011) and VIIRS (2012–2023) records introduces a risk of inconsistency; the higher detection sensitivity of VIIRS could result in an artificial increase in fire counts, which might be misinterpreted as a real upward trend in global fire activity. To maintain the homogeneity of the 21-year dataset for trend analysis, we prioritized sensor consistency. We acknowledge that this choice likely leads to an underestimation of emissions from small-scale agricultural fires, particularly in regions like the Middle East or India, where fires are often smaller than the MODIS detection threshold (Hantson et

al., 2013; Justice et al., 2002; Vadrevu and Lasko, 2018).

3. To address the limitation of a static AGB benchmark map, net primary productivity (NPP) is used as a proxy to generate annual global AGB maps. Does this approach introduce inherent uncertainties? The authors should discuss these.

Response: We sincerely appreciate the reviewer's critical assessment regarding the uncertainties associated with the fuel load estimation methodology. We fully acknowledge that the derivation of dynamic annual Aboveground Biomass (AGB) from static baseline maps using Net Primary Productivity (NPP) as a proxy is a methodological simplification that inevitably introduces inherent uncertainties into the bottom-up inventory. As correctly highlighted by the reviewer, and as we have now explicitly discussed in the revised manuscript, the relationship between these two variables is ecologically complex; fundamentally, AGB represents a cumulative carbon stock, whereas NPP represents an annual carbon flux. Consequently, their correlation is influenced by non-linear factors such as ecological lag effects, variable tree mortality rates, and decomposition processes, meaning that a year of high NPP does not necessarily translate into an immediate, proportional increase in standing biomass.

However, the decision to adopt this NPP-based proxy method was driven by the stringent constraints of current data availability. For the study period of 2003–2023, there exists no continuous, global, high-resolution annual AGB observational dataset. Faced with the choice between using a completely static AGB map—which would erroneously assume constant fuel loads despite significant climate variability—and using an NPP-driven dynamic adjustment, we determined that the latter represents the most scientifically robust available strategy to approximate the interannual variability of fuel availability, despite its physical limitations.

In response to the reviewer's suggestion, we have expanded Section 4.2 (Limitations and Future Perspectives) to include a dedicated discussion on these specific uncertainties. We clarified that while this approach allows us to capture the directional trends of interannual fuel dynamics, it remains a surrogate method. We further elaborated that future iterations of the MBEI aim to overcome this reliance on proxies by integrating direct vertical structure measurements from next-

generation active remote sensing missions, such as NASA GEDI and ESA BIOMASS, once long-term records from these sensors become available to directly resolve dynamic fuel loads.

Please refer to Page 30, Lines 673-683 and the following is the revised manuscript:

Advancements in next-generation satellites will also enhance the MBEI's capacity for fuel load estimation. In this study, due to the lack of high-resolution annual AGB observations, we adjusted static AGB maps using interannual variations in NPP. However, AGB is a cumulative stock variable, whereas NPP is an annual flux variable. Their relationship is complex and influenced by factors such as lag effects, tree mortality, and decomposition, meaning a high NPP year does not always result in an immediate biomass increase (Keeling and Phillips, 2007; Teets et al., 2022). Future versions of MBEI aim to improve this by integrating dynamic AGB datasets from active remote sensing missions. Specifically, spaceborne LiDAR (e.g., NASA GEDI) and P-band SAR (e.g., ESA BIOMASS mission) are expected to provide global measurements of forest vertical structure. This will allow MBEI to incorporate dynamic fuel loads, thereby reducing a major source of uncertainty in the bottom-up approach based on burned area (Cao et al., 2016; Liu et al., 2019; Rodríguez-Fernández et al., 2018).

4. The abstract is overly long and information-dense. I suggest to keep the most important findings and shorten the abstract to make the expression more concise.

Response: We sincerely appreciate the reviewer's constructive feedback regarding the length and density of the abstract. We fully acknowledge that the original text, while comprehensive, was overly verbose in its contextualization and methodological detailing, which may have diluted the immediate impact of the study's core contributions. We have accepted this suggestion and performed a rigorous editorial revision to significantly condense the abstract, thereby enhancing its concise expression and readability while retaining the most critical scientific findings.

In the revised abstract, we have streamlined the narrative structure to prioritize the research gap and our specific contributions. First, we excised the generic background information regarding global climate change to focus immediately on the critical issue of discrepancies among existing inventories. Second, we compressed the methodological description; rather than listing every

specific atmospheric pollutant, we focused on the innovative nature of the "ensemble framework" that integrates bottom-up and top-down approaches to quantify structural uncertainty. This allowed us to dedicate more space to the key empirical findings, which have been sharpened for clarity. Specifically, we retained the crucial quantitative results—such as the two-fold difference between maximum and minimum global estimates—and the distinct spatial heterogeneity of uncertainty, highlighting the contrast between high-uncertainty regions like Australia and lower-uncertainty regions like Africa. Furthermore, we refined the description of the temporal trends to clearly articulate the identified decadal shift: a decline in tropical burning (2003–2013) followed by a resurgence driven by high-latitude fires (2013–2023). These revisions ensure that the abstract now directly and effectively communicates the MBEI's value in providing robust central estimates and explicit uncertainty bounds for atmospheric modeling.

Q5: The Discussion section should be strengthened. Other factors are likely to bring the uncertainty in the estimation of biomass burning emission, for example the omission and commission errors in the satellite fire observations. Meanwhile, the existing bottom-up and up-down method is like to underestimate the emission for small-scale fire.

Please refer to Page 2, Lines 36-50 and the following is the revised manuscript:

Abstract. Large discrepancies among existing inventories hinder a consensus on the true magnitude and long-term trends of global biomass burning emissions. To address this, we developed the Multi-ensemble Biomass-burning Emissions Inventory (MBEI), a framework integrating bottom-up and top-down approaches with multi-source data to generate eight sub-inventories for the period 2003–2023. This ensemble approach allows for the explicit quantification of emission uncertainty at a 0.1° grid scale. We estimate global annual CO₂ emissions at 7304 (4400–9657) Tg, with the maximum estimate exceeding the minimum by over two-fold. The uncertainty exhibits significant spatial heterogeneity: it is highest in low-emission regions like Australia and the Middle East (6.0–7.0 fold difference), whereas traditional hotspots like Africa show lower divergence (Approximately 2 fold). Temporally, a distinct decadal shift was identified: global emissions declined from 2003 to 2013 due to reduced tropical burning, but reversed to an increasing trend from 2013 to 2023, driven by intensified fires in northern high-latitudes and extreme events. Comparisons confirm that the MBEI mean provides a robust central estimate, while its max-min range effectively encompasses other

major inventories. By providing explicit uncertainty bounds, MBEI enhances the reliability of atmospheric modeling and climate assessments. The dataset is publicly available at <https://doi.org/10.5281/zenodo.17128279> (Liu and Yin, 2025).

5. The Discussion section should be strengthened. Other factors are likely to bring the uncertainty in the estimation of biomass burning emission, for example the omission and commission errors in the satellite fire observations. Meanwhile, the existing bottom-up and up-down method is like to underestimate the emission for small-scale fire.

Response: We sincerely appreciate the reviewer's constructive critique regarding the comprehensiveness of our discussion on uncertainty sources. We fully agree with the reviewer's assessment that beyond the structural uncertainties arising from algorithm choice, the fundamental physical limitations of satellite observations—specifically omission errors related to detection thresholds for small-scale fires—constitute significant sources of bias that necessitate rigorous examination. We acknowledge that existing bottom-up and top-down methods share these inherent physical constraints, which often lead to a systematic underestimation of emissions in specific fire regimes.

In direct response to this suggestion, we have substantially strengthened Section 4.2 to provide a deep-dive analysis of these physical limitations. A central focus of this revision is the explicit discussion of the trade-offs involved in sensor selection and the consequent impact on small-fire detection. We clarified that a key decision in this study was to use MODIS active fire products (MCD14DL) exclusively for the 2003–2023 period to ensure trend validity. We argue that although the Visible Infrared Imaging Radiometer Suite (VIIRS), available since 2012, offers superior spatial resolution (375 m) compared to MODIS (1 km), applying it would have limited the consistent time series to the post-2012 era. Furthermore, merging MODIS (2003–2011) and VIIRS (2012 – 2023) records introduces a substantial risk of inconsistency; the higher detection sensitivity of VIIRS could result in an artificial increase in fire counts, which might be misinterpreted as a real upward trend in global fire activity. To maintain the homogeneity of the 21-year dataset for trend analysis, we prioritized sensor consistency. However, in the revised discussion, we explicitly acknowledge that

this choice likely leads to an underestimation of emissions from small-scale agricultural fires, particularly in regions like the Middle East or India, where fires are often smaller than the MODIS detection threshold.

In addition to sensor resolution, we also expanded the text to address omission errors driven by environmental heterogeneity, such as subsurface peat smoldering and canopy occlusion, which further constrain detection capabilities. By articulating these mechanisms, we highlight that the MBEI, while robust, is still bound by the physics of the input sensors. To conclude this discussion, we emphasized the adaptability of our system: in conclusion, while the current version of MBEI quantifies uncertainty by integrating established methods, its modular design serves as a platform for incorporating new data inputs as they become available. This ensures a feasible pathway for iterative refinement, supporting more comprehensive assessments of global biomass burning emissions.

Please refer to Page 29-30, Lines 643-672 and the following is the revised manuscript:

A key decision in this study was to use MODIS active fire products (MCD14DL) exclusively for the 2003–2023 period. Although the Visible Infrared Imaging Radiometer Suite (VIIRS), available since 2012, offers superior spatial resolution (375 m) compared to MODIS (1 km), applying it would have limited the consistent time series to the post-2012 era. Merging MODIS (2003–2011) and VIIRS (2012–2023) records introduces a risk of inconsistency; the higher detection sensitivity of VIIRS could result in an artificial increase in fire counts, which might be misinterpreted as a real upward trend in global fire activity. To maintain the homogeneity of the 21-year dataset for trend analysis, we prioritized sensor consistency. We acknowledge that this choice likely leads to an underestimation of emissions from small-scale agricultural fires, particularly in regions like the Middle East or India, where fires are often smaller than the MODIS detection threshold (Hantson et al., 2013; Justice et al., 2002; Vadrevu and Lasko, 2018).

In addition to sensor specifications, most current inventories relying on optical remote sensing face inherent physical limits driven by environmental heterogeneity. Complex surface conditions can constrain the effectiveness of estimation methods. For instance, in the peatlands of Equatorial Asia (e.g., Indonesia), fires often occur as subsurface low-temperature smoldering. The thermal radiation from these fires is frequently too weak to trigger standard satellite detection algorithms (Rein and Huang, 2021;

Sofan et al., 2019). Similarly, in dense tropical rainforests, the canopy layer can occlude or absorb thermal radiation emitted by understory fires (East et al., 2023). These scenarios contribute to omission errors in top-down, FRP-based approaches (Morton et al., 2013; Tyukavina et al., 2022). Conversely, while bottom-up methods based on burned area can capture the spatial traces of these fires, they face challenges in accurately determining the depth of burn in organic soils (Ballhorn et al., 2009; Wiggins et al., 2018). Therefore, despite the integration of multiple algorithms in MBEI, these physical constraints suggest a potential underestimation in our emission estimates for these specific biomes.

Looking forward, the flexible architecture of MBEI is designed to incorporate emerging datasets to address these limitations. As the observational record of VIIRS extends, future versions of MBEI will integrate these data to improve the detection of small-scale fires once a sufficiently long and consistent record is established. Furthermore, data from new-generation geostationary satellites (e.g., FY-4, Himawari-8/9, GOES-R) offer a significant improvement in temporal resolution. Minute-level observations from these platforms will enable the direct integration of the Fire Radiative Power (FRP) diurnal cycle, reducing the reliance on Gaussian extrapolation from sparse polar-orbiter snapshots and enhancing the physical realism of Fire Radiative Energy (FRE) estimation.

Minor comments:

1. Line 67-68: add references to support this statement.

Response: We sincerely thank the reviewer for pointing out the need for supporting citations to substantiate this foundational statement. We agree that referencing authoritative literature is essential for establishing the context of biomass burning as a key ecosystem disturbance. Accordingly, we have inserted citations to Bowman et al. (2020) and Jones et al. (2022) in the revised manuscript to support the text: "Biomass burning, encompassing forest fires, grassland fires, and the burning of agricultural residues, is a key disturbance in terrestrial ecosystems."

Please refer to Page 3, Lines 69-70 and the following is the revised manuscript:

Biomass burning, encompassing forest fires, grassland fires, and the burning of agricultural residues, is a key disturbance in terrestrial ecosystems (Bowman et al., 2020; Jones et al., 2022).

2. Lines 90–91: An extraneous period appears after “Karanasiou et al (2021)”. Please remove it to ensure proper punctuation.

Response: We appreciate the reviewer’s meticulous attention to detail regarding punctuation. We have removed the extraneous period following "Karanasiou et al. (2021)" to ensure grammatical correctness and proper sentence flow.

Please refer to Page 3, Lines 92 and the following is the revised manuscript:

[A meta-analysis of 81 studies \(1980–2020\) \(Karanasiou et al., 2021\).](#)

3. There are some grammar issues and please proofread the entire manuscript carefully before resubmission. For example, Line 102-103, “Atmospheric Chemistry Transport Models used for air quality forecasting and source apportionment, rely on emission inventories with high spatiotemporal resolution and reliability”.

Response: We apologize for the grammatical oversight in Lines 102–103 and for any other linguistic imperfections in the original draft. We have corrected the specific sentence to read: "Atmospheric Chemistry Transport Models, which are used for air quality forecasting and source apportionment, rely on emission inventories with high spatiotemporal resolution and reliability." Furthermore, prior to this resubmission, we have conducted a comprehensive proofreading of the entire manuscript to eliminate grammatical errors and enhance the overall clarity and fluency of the English text.

Please refer to Page 3, Lines 92 and the following is the revised manuscript:

[Atmospheric Chemistry Transport Models, which are used for air quality forecasting and source apportionment, rely on emission inventories with high spatiotemporal resolution and reliability.](#)

4. Line 182: The current format is cluttered and hard to read. Please reformat it.

Response: We thank the reviewer for noting the formatting issues in Table 1. We agree that a cluttered presentation hinders readability and have therefore completely reformatted Table 1. The revised table now presents the dataset information in a clean, organized, and reader-friendly manner.

Please refer to the following is the revised Table 1:

Table 1. Datasets used in this study.

Data types	Name	Temporal Coverage	Spatial Resolution	Temporal Resolution	Reference
Active Fire Data	Aqua MCD14DL	2003-2023	1 km × 1 km	daily	(NASA VIIRS Land Science Team, 2021)
	Terra MCD14DL	2003-2023	1 km × 1 km	daily	(NASA VIIRS Land Science Team, 2021)
Burning Efficiency (BE) & Emission Factor (EF) Data	EF Classification Source Data GFED	\	0.25° × 0.25°	\	(van der Werf et al., 2006)
	EF Coefficients	\	\	\	(van der Werf et al., 2017)
AGB Data	BE Coefficients	\	\	\	(Shi et al., 2015)
	GlobBiomass	2010	25 m × 25 m	\	(Santoro, 2018)
	Biomass_cci	2010/2015-2021	100 m × 100 m	yearly	(Santoro and Cartus, 2024)
Conversion Factor (CR) Data	30-class CR map	\	0.1° × 0.1°	\	(Kaiser et al., 2023)
	8-class CR map	\	0.1° × 0.1°	\	(Kaiser et al., 2012)
Ancillary & Validation Data	Net Primary Production (NPP) MYD17A3HGF v061	2003-2023	500 m × 500 m	yearly	(Running and Zhao, 2021)
	Land Cover Type MCD12Q1.061	2003-2023	500 m × 500 m	yearly	(Friedl and Sulla-Menashe, 2022)
Validation Inventory Data	Global Fire Emissions Database 5 (GFED 5)	2003-2022	0.25° × 0.25°	daily	(Binte Shahid et al., 2024; Vernooij et al., 2023; Wiggins et al., 2021)
	Fire INventory from NCAR 2.5 (FINN 2.5) MODIS	2002-2022	0.1° × 0.1°	daily	(Wiedinmyer et al., 2023)
	Global Fire Assimilation System 1.2 (GFAS 1.2)	2003-2022	0.1° × 0.1°	daily	(Kaiser et al., 2012)
	Quick Fire Emissions Dataset 3.1 (QFED 3.1)	2003-2022	0.1° × 0.1°	daily	(Koster et al., 2015)

Note: The 8-class biome map is derived from the 30-class biome map. See Fig. S1 for its spatial distribution.

5. Figures 2a and 3a,b: Fonts are too small, reducing readability. Please enlarge them and ensure consistent styling across panels.

Response: We appreciate the reviewer’s feedback regarding the visual clarity of our figures. We acknowledge that the font sizes in Figures 2a and 3a,b were insufficient for easy reading. We have redrawn these panels with significantly enlarged fonts and have ensured that the styling is consistent across all figures to improve the overall graphical quality of the manuscript.

Please refer to the following is the revised Figure 2 and 3:

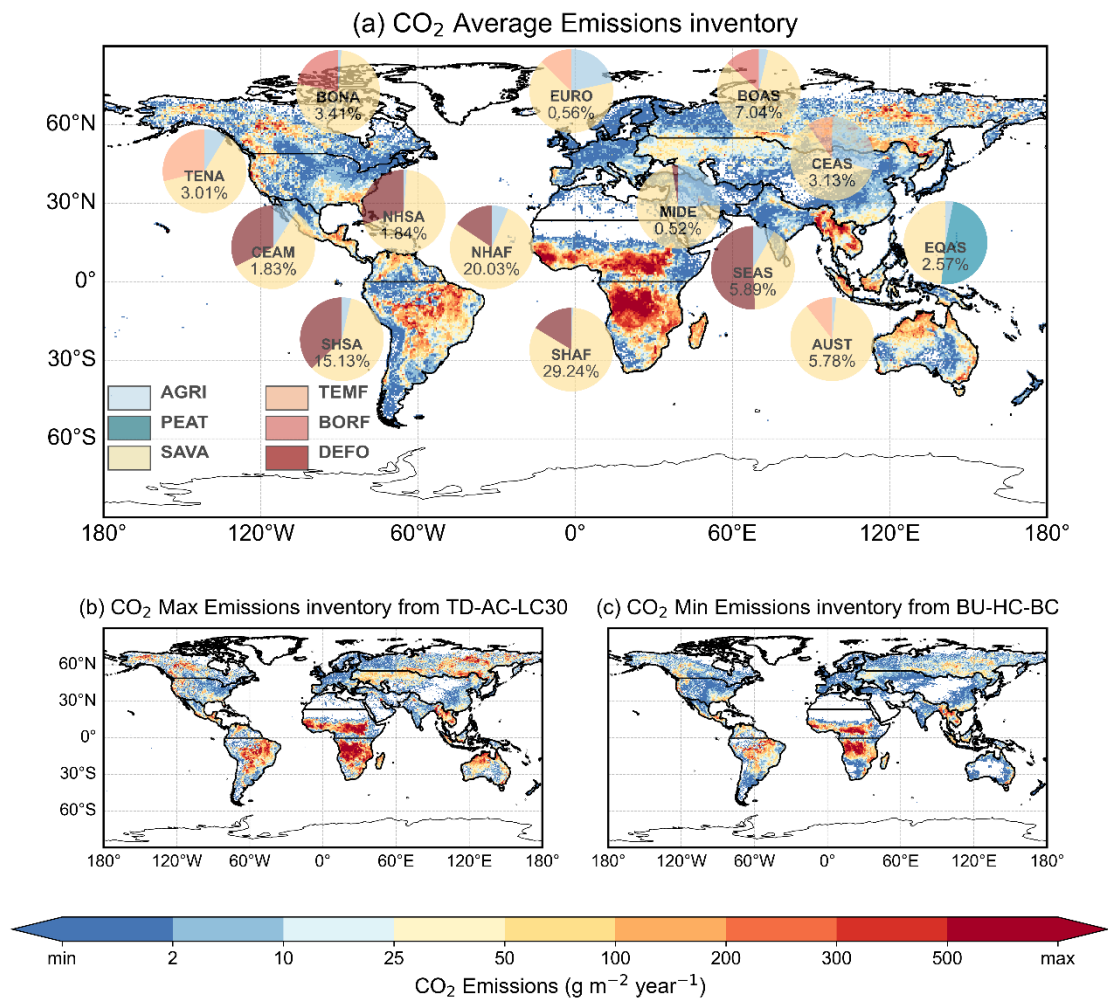


Figure 2. Spatial patterns and regional composition of global biomass burning CO₂ emissions (mean of 2003–2023). (a) Spatial distribution of the annual mean CO₂ emission flux estimated from the mean of the eight inventories in this study. The embedded pie charts show the emission composition for 14 major regions, where: 1) the number in the pie chart indicates the percentage of that region's emissions relative to the global total; and 2) the sectors of the pie chart represent

the proportional contribution of six major fire types to the region's total emissions. (b) and (c) show the spatial emission patterns corresponding to the inventory with the highest global total annual emissions (TD-AC-LC30) and the lowest global total annual emissions (BU-HC-BC) among the eight inventories over the entire study period, respectively.

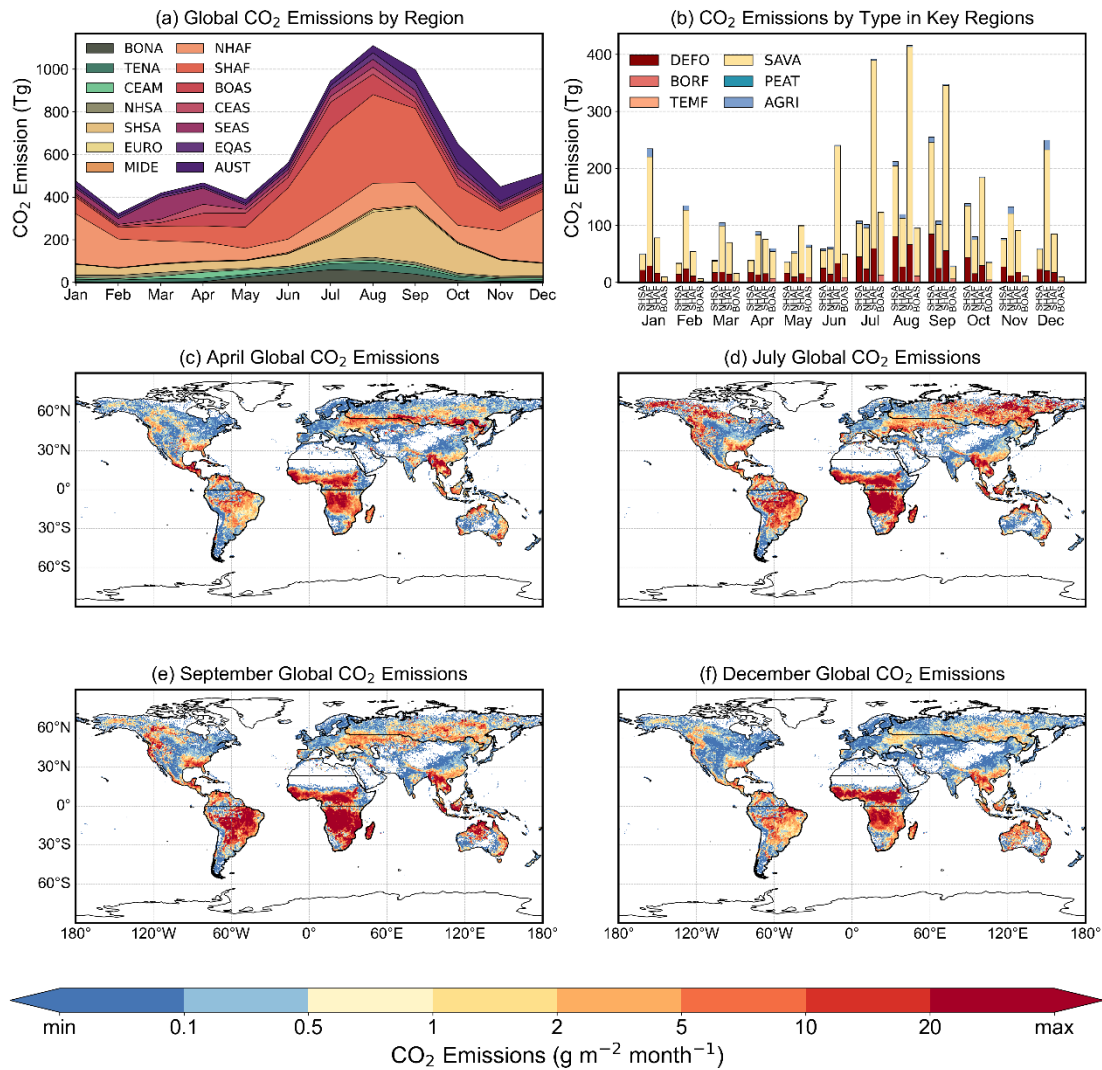


Figure 3. Seasonal cycle and spatial dynamics of global biomass burning CO₂ emissions (mean of 2003–2023). (a) Global monthly emissions partitioned by source region. (b) Monthly emissions for the four primary contributing regions, showing the composition by fire type. (c-f) Spatial distribution of mean monthly emission flux during key seasonal phases: April, July, September, and December.

6. Two extraneous spaces appear between “high” and “biomass”. Please delete them for clean typesetting.

Response: We thank the reviewer for spotting this typographical error. We have removed the extraneous

spaces between "high" and "biomass" to ensure clean and professional typesetting. The sentence now correctly reads: "Importantly, high biomass burning emission uncertainty is not found in traditional biomass burning hotspots."

Please refer to Page 17, Lines 396 and the following is the revised manuscript:

Importantly, high biomass burning emission uncertainty is not found in traditional biomass burning hotspots. Instead, some of the highest uncertainties are found in regions with lower overall emissions.

7. Table 3: please do not use the short name for maximum, minimum, and average.

Response: We accept the reviewer's suggestion to use formal terminology in our data presentation. We have revised the headers in Table 3 to use the full terms "Maximum," "Minimum," and "Average" instead of abbreviations, ensuring clarity and adherence to academic standards.

Please refer to the following is the revised Table 3:

Table 3. Total annual CO₂ emissions (Maximum, Minimum, and Average, unit: Tg) for 2003–2023.

Year	Maximum	Minimum	Average	Year	Maximum	Minimum	Average
2003	10882.90	4487.65	7673.68	2014	9258.62	4489.87	7265.29
2004	10842.08	4271.50	7522.16	2015	9688.74	5035.46	7701.46
2005	10391.58	4350.62	7328.15	2016	8476.61	4059.68	6789.30
2006	9663.37	4160.83	7077.83	2017	9250.64	4436.15	7042.77
2007	11063.35	4641.22	7751.48	2018	8727.34	4160.93	6911.22
2008	9725.05	4030.68	6925.95	2019	9747.60	4971.22	7657.46
2009	8661.02	3930.36	6669.83	2020	9295.62	4375.98	7249.50
2010	10253.23	4748.50	7554.59	2021	10696.69	4767.44	7705.11
2011	9653.73	4119.74	7205.26	2022	7289.55	3348.45	6442.83
2012	10537.30	4721.32	7895.63	2023	10527.88	5206.72	8506.96
2013	8161.82	4087.36	6489.87	Mean	9656.89	4400.08	7303.16

8. Line 469: use a consistent format for the term "max-min band".

Response: We appreciate the reviewer's guidance on maintaining terminological consistency. We have carefully reviewed the entire manuscript and standardized the usage of the term "max-min band"

throughout the text to avoid any confusion.

Please refer to Page 22, Lines 475 and the following is the revised manuscript:

Alongside these climate-driven variations, the MBEI is characterized by a broad uncertainty range, stemming from differences in algorithm structures and input data. The spread between MBEI estimates (the max-min band in Figs. 4a, c, e) is considerable, with the difference between the highest and lowest annual totals exceeding 2600 Tg in some years (e.g., 2004, 2022).

9. Line 477-479: Is there any tables or figures in the supplementary material to support these results?

Response: We thank the reviewer for suggesting the inclusion of supporting data for these results. We agree that providing the underlying data enhances the robustness of our claims. Therefore, we have added new supplementary tables (Table S6–S8) to the Supplementary Material, which explicitly support the results discussed in Lines 477–479.

Please refer to Page 22-23, Lines 482-512 and the following is the revised manuscript:

Over the full 21-year period, statistically significant trends were concentrated in Asia. BOAS exhibited a strong and significant increasing trend in emission flux at a rate of 15.71 g m⁻² yr⁻¹ ($p < 0.01$). In contrast, CEAS and SEAS showed significant decreasing trends of -1.72 g m⁻² yr⁻¹ ($p < 0.01$) and -2.08 g m⁻² yr⁻¹ ($p < 0.05$), respectively (Table. S6). Fig. 4b suggests decreases in equatorial Africa and central-southern South America, and increases in BONA, these trends were not statistically significant when aggregated over the entire 14 GFED regions for the 2003–2023 period. This highlights an offsetting pattern, where declining emissions in some regions are partially balanced by increases elsewhere, contributing to the lack of a significant global trend.

A decadal comparison between 2003–2013 and 2013–2023 reveals substantial evolution in these spatial patterns, indicating a major shift in the global distribution of biomass burning emissions (Figs. 4d, f).

During the first decade (2003–2013), a slight but statistically non-significant global decrease ($p > 0.05$; Fig. 4c) masked a profound spatial redistribution of fire activity. The dominant feature was a significant increase in fire emissions in SHAF, which saw an upward trend of 4.41 g m⁻² yr⁻¹ ($p < 0.05$). By contrast, South America experienced significant decreases, particularly in NHSA where emissions declined at a rate of -4.97 g m⁻² yr⁻¹ ($p < 0.05$). Simultaneously, a strong decreasing trend was observed in CEAS,

with a rate of $-2.96 \text{ g m}^{-2} \text{ yr}^{-1}$ ($p < 0.05$). Boreal regions and Southeast Asia showed no statistically significant regional trends during this period (Fig. 4d and Table. S7).

In the subsequent decade (2013–2023), this pattern shifted markedly. Although the global emission trajectory did not exhibit a statistically significant linear trend ($p > 0.05$), it transitioned from a slight decline to an overall increase (Fig. 4e), signaling a clear decadal change in biomass burning dynamics. This shift is more appropriately characterized as a structural transformation rather than a linear progression, driven by a marked increase in both the frequency and intensity of extreme emission years (e.g., 2015, 2019, 2023). The 2015–2016 ENSO cycle exemplifies this mechanism, as the super El Niño event in 2015 induced catastrophic PEAT in Indonesia (EQAS) and elevated global emissions to a record peak, which was subsequently followed by a pronounced decline in 2016 with the onset of a strong La Niña (Whitburn et al., 2016; Yin et al., 2020a). The 2023 fire season was even more pronounced, as an unprecedented wildfire season in boreal Canada (BONA) coincided with a developing El Niño, jointly driving global annual emissions to the highest level in our 21-year record and Detailed regional statistics, including the annual mean CO₂ emission fluxes and their corresponding Theil-Sen slope trends across the 14 study regions for the 2013–2023 period, are summarized in Table S8 (Jain et al., 2024; Luo et al., 2025).

Please refer to the following is the revised Table S6-8:

Table S6. Mean annual CO₂ emission fluxes and their corresponding Theil-Sen slope trends across 14 regions from 2003 to 2023. (unit: g m^{-2}).

Region	Mean Emission Flux	Theil Sen Slope value
BONA	543.72	12.12
TENA	114.04	2.67
CEAM	98.28	-0.61
NHSA	115.33	1.06
SHSA	173.34	1.24
EURO	52.05	-0.02
MIDE	77.65	0.64
NHAF	266.74	0.37
SHAF	330.52	1.24
BOAS	371.02	15.71
CEAS	56.89	-1.72
SEAS	137.16	-2.08
EQAS	163.81	-4.78
AUST	195.02	-1.30

Table S7. Mean annual CO₂ emission fluxes and their corresponding Theil-Sen slope trends across 14 regions from 2003 to 2013. (unit: g m⁻²).

Region	Mean Emission Flux	Theil Sen Slope value
BONA	418.62	-4.65
TENA	99.06	0.73
CEAM	103.17	-0.10
NHSA	105.58	-4.97
SHSA	170.75	-6.13
EURO	44.50	-1.11
MIDE	73.12	0.09
NHAF	264.05	2.57
SHAF	325.09	4.41
BOAS	279.94	9.10
CEAS	61.30	-2.96
SEAS	150.13	-0.02
EQAS	172.99	-6.91
AUST	195.80	0.44

Table S8. Mean annual CO₂ emission fluxes and their corresponding Theil-Sen slope trends across 14 regions from 2013 to 2023. (unit: g m⁻²).

Region	Mean Emission Flux	Theil Sen Slope value
BONA	663.77	11.93
TENA	128.43	3.78
CEAM	94.85	0.47
NHSA	123.83	3.72
SHSA	170.02	8.01
EURO	58.03	-0.30
MIDE	80.63	0.61
NHAF	269.14	-5.14
SHAF	337.60	-1.77
BOAS	460.83	17.48
CEAS	50.72	-0.30
SEAS	125.39	-2.72
EQAS	154.30	-11.19
AUST	189.94	0.85

10. Supplementary material: Please ensure all figures and tables are explicitly referenced in the main text.

Response: We appreciate this important reminder regarding the linkage between the main text and the supplementary information. We have performed a systematic check of the manuscript to ensure that every

figure and table included in the Supplementary Material is explicitly and correctly referenced within the main text.

Responds to the reviewer's comments:

Reviewer #2:

1. How were the considerations addressed for the selection of multi-source data in this study? Specifically, as shown in Table 1, the temporal resolutions of the listed data sources vary significantly. How were annual-average data interpolated into monthly-average values?

Response: We appreciate the reviewer's keen attention to the data selection process and the methodological details concerning temporal resolution handling. We have carefully revised the manuscript to clarify that our approach does not involve simple temporal interpolation of annual averages; rather, it employs a mechanism that synthesizes static inputs with dynamic proxies to reconstruct continuous emission timelines, a necessity driven by the current availability of global biomass datasets.

Regarding the considerations for multi-source data selection, our primary rationale was to construct an ensemble framework capable of quantifying structural uncertainties by incorporating independent, high-quality datasets. As detailed in the revised Table 1, we selected the GlobBiomass and Biomass_cci datasets to drive the bottom-up stream. The GlobBiomass dataset provides a static baseline for the year 2010, generated through an innovative fusion of spaceborne SAR, LiDAR, and optical observations. The Biomass_cci dataset offers estimates for specific years (2007, 2010, and annually from 2015 to 2022), derived from a combination of Copernicus Sentinel-1, Envisat's ASAR, and JAXA's ALOS missions. However, a critical challenge in long-term biomass emission modeling is the absence of a high-resolution, spatially continuous AGB dataset that covers every single year of the entire study period (2003–2023). Existing high-precision products are either static baselines or cover discontinuous time intervals, making them insufficient for directly driving a continuous twenty-year inventory without temporal reconstruction.

Consequently, to address this data gap and capture the interannual variability of fuel loads, we implemented the dynamic derivation method described in Section 2.2.1. Specifically, we first transformed the static baseline AGB maps into dynamic annual AGB datasets by leveraging the interannual variability of Net Primary Production (NPP), based on the ecological relationship

described in Equation (1). This dynamic annual AGB, combined with annual Land Cover-derived parameters, allows us to calculate the total Annual Emissions (EM) for each grid cell using Equation (3). This step ensures that the magnitude of emissions is constrained by the actual annual fuel load and vegetation conditions of that specific year, without artificially smoothing the data across months. Subsequently, to achieve the monthly resolution required for the inventory, we implemented a temporal downscaling mechanism driven by high-frequency satellite observations. As defined in Equation (4), the total annual emission calculated in the previous step is allocated to specific months in direct proportion to the monthly cumulative Fire Radiative Power (FRP). Satellite-observed FRP serves as a high-fidelity proxy for instantaneous combustion intensity and timing. Therefore, while the quantity of biomass available for burning is governed by the annual datasets (AGB and NPP), the seasonality and precise timing of the emissions are dictated by the monthly distribution of real-time fire radiative energy. This methodology effectively bridges the gap between the coarse temporal resolution of fuel load data and the high temporal resolution of fire activity, ensuring that the final monthly inventory reflects both accurate biological fuel constraints and precise satellite-detected fire dynamics. We have explicitly refined the text in Section 2.2.1 to articulate this stepwise mechanism and remove any ambiguity regarding the treatment of temporal resolutions.

Overall, we utilized the relative interannual variations in MODIS Net Primary Production (NPP) to extrapolate the baseline AGB maps for years where direct observations were unavailable. We explicitly acknowledge, as discussed in Section 4.2, that this approach serves as a necessary proxy given current observational limitations; conceptually, AGB is a cumulative stock variable while NPP is an annual flux variable, and their relationship is complex due to lag effects and decomposition. Future versions of MBEI aim to improve this limitation by integrating dynamic AGB datasets from active remote sensing missions. Specifically, spaceborne LiDAR (e.g., NASA GEDI) and P-band SAR (e.g., ESA BIOMASS mission) are expected to provide global measurements of forest vertical structure, which will allow MBEI to incorporate dynamic fuel loads directly. However, pending the availability of such long-term continuous records, the use of NPP-driven interannual adjustment currently represents the most robust available method to approximate annual fuel load dynamics from static or sparse baselines.

Please refer to Page 11-12, Lines 258-295 and the following is the revised manuscript:

This study employs a bottom-up method, combining multi-source remote sensing data to construct four global monthly biomass burning emission inventories for 2003–2023. The core computational workflow involves four key steps: (1) constructing a dynamic annual AGB dataset based on interannual variations in NPP; (2) modeling the total burned dry matter density (BD) under multiple fire events within a year; (3) estimating total annual emissions (EM) by burned area (BA), BD and EF; (4) downscaling annual emissions to a monthly resolution using the monthly distribution of FRP.

To overcome the limitation of using a static AGB benchmark map that ignores interannual variability, we constructed a dynamic annual AGB dataset. Based on the ecological assumption of a stable proportional relationship between AGB and NPP (Raich et al., 2006; Whittaker and Likens, 1972), we used the relative interannual changes in the MODIS annual NPP product to extrapolate the baseline AGB. The AGB for a target year (m) in a specific pixel (p) is calculated as:

$$AGB_{(m,p)} = AGB_{(a,p)} \times \frac{NPP_{(m,p)}}{NPP_{(a,p)}} \quad (1)$$

where $AGB_{(m,p)}$ is the AGB in year m at pixel p ($Mg\ ha^{-1}$); $AGB_{(a,p)}$ is the baseline AGB at pixel p (mean of 2003–2023, $Mg\ ha^{-1}$); $NPP_{(m,p)}$ is the NPP in year m at pixel p ($kg\ C\ m^{-2}\ yr^{-1}$); and $NPP_{(a,p)}$ is the baseline mean NPP at pixel p ($kg\ C\ m^{-2}\ yr^{-1}$).

After obtaining annual AGB, we estimated the annual BD per unit area. Considering that a pixel may experience multiple fires in a year, we used the following model to simulate the sequential consumption of AGB by fire and accumulate the total annual burned amount:

$$BD_{(m,p)} = \sum_{j=1}^I \{AGB_{(m,p)} \times (1-BE_c)^{j-1} \times BE_c\} \quad (2)$$

where $BD_{(m,p)}$ is the total burned dry matter density in year m at pixel p ($kg\ m^{-2}$); I is the fire frequency in year m at pixel p (derived from active fire data); j represents the j -th fire event of the year; $AGB_{(m,p)}$ is the initial AGB at the beginning of the year ($kg\ m^{-2}$); and BE_c is the dimensionless burning efficiency for the land cover type c of pixel p (derived from the Land Cover Type MCD12Q1.061).

The total annual emissions of each pollutant are estimated based on the method proposed by Seiler

and Crutzen (1980):

$$EM_{(m,p)} = BA_{(m,p)} \times BD_{(m,p)} \times EF \quad (3)$$

where $EM_{(m,p)}$ is the annual emission of a specific pollutant in year m at pixel p (g); $BA_{(m,p)}$ is the total annual burned area in year m at pixel p (m^2), obtained by multiplying the annual MODIS active fire location mask by the pixel's geographic area to ensure that the burned location is consistent with fire detections; $BD_{(m,p)}$ is the annual burned dry matter density ($kg\ m^{-2}$) calculated from Eq. (2); and EF is the emission factor for the specific pollutant ($g\ kg^{-1}$). It is important to note that inputs with annual temporal resolution (e.g., AGB, Land Cover-derived BE and EF) determine the magnitude of $EM_{(m,p)}$ in this step and are not interpolated.

Finally, to obtain a monthly-resolution emission inventory, we applied a temporal allocation approach. We used satellite-observed FRP as a high-frequency proxy for fire activity intensity to distribute the total annual emissions $EM_{(m,p)}$ into each month (t):

$$EM_{(m,p,t)} = EM_{(m,p)} \times \frac{FRP_{(m,p,t)}}{\sum_{t=1}^{12} FRP_{(m,p,t)}} \quad (4)$$

where $EM_{(m,p,t)}$ is the pollutant emission in month t of year m at pixel p (g); and $FRP_{(m,p,t)}$ is the monthly cumulative FRP in month t of year m at pixel p ($MJ\ s^{-1}$). This method ensures that while the total emission magnitude is constrained by annual fuel loads, the seasonality is driven by real-time fire radiative observations.

2. Section 2.2 provides detailed descriptions of the bottom-up and top-down approaches. However, the explanation of the integrated approach employed in this study remains insufficiently clear. Please provide further clarification.

Response: We sincerely appreciate the reviewer's rigorous scrutiny regarding the conceptual framing of our integration methodology. We acknowledge that the initial description of the "integrated approach" may have inadvertently implied a conventional data fusion mode, rather than the ensemble framework actually employed. We have accepted this comment and completely

rewritten the introductory paragraph of Section 2.2 to explicitly clarify that the Multi-source Biomass Emission Inventory (MBEI) is constructed as a multi-model ensemble system designed to quantify structural uncertainty through a combinatorial design, rather than a single fused algorithm.

To resolve the ambiguity, we clarified that the "integration" in this study refers to the parallel execution and subsequent statistical aggregation of eight independent emission sub-inventories, generated through a rigorous permutation of key input variables. Specifically, the framework operates by establishing two distinct methodological streams. For the bottom-up, which relies on burned area and fuel load dynamics, we generated four distinct sub-inventories by cross-referencing two independent Aboveground Biomass datasets (GlobBiomass and Biomass_cci) with two active fire screening criteria (one including all detected fires and another restricted to medium-to-high confidence detections). Similarly, for the top-down driven by Fire Radiative Energy we produced four corresponding sub-inventories by combining two distinct Conversion Ratio schemes (based on 8-class and 30-class biome maps) with the same two fire confidence filtering levels. This 2×2 combinatorial design within both methods results in a total matrix of eight parallel sub-inventories for every 0.1° grid cell.

Furthermore, the core logic of our framework is not to obscure the discrepancies between these sub-inventories, but to preserve them as a measure of reliability. We explicitly recognize that differences in input data (e.g., AGB sources) and estimation methodologies (bottom-up vs. top-down) inevitably lead to substantial variations in emission estimates. Rather than eliminating these divergences through data assimilation, the MBEI retains the full spread of the eight sub-inventories to compute grid-scale ensemble statistics, including the mean, standard deviation, minimum, and maximum values. We posit that preserving these differences is essential for scientific objectivity, as the dispersion among the sub-inventories directly reflects the structural uncertainty inherent in current biomass burning observation capabilities. This revision in Section 2.2 ensures precise terminology and clearly articulates how the ensemble framework utilizes these methodological branches to construct a transparent and probabilistically bounded assessment of global emissions.

Please refer to Page 10, Lines 243-252 and the following is the revised manuscript:

To quantify global biomass burning emissions and their associated uncertainties, we constructed the

MBEI using a multi-source ensemble framework. Unlike conventional approaches that rely on a single algorithm, this framework operates by generating an ensemble of eight independent sub-inventories (see Table 2). This design is explicitly structured to capture the structural uncertainty stemming from the fundamental mechanistic discrepancies between bottom-up (burned area-based) and top-down (fire radiative power-based) methodologies. Rather than obscuring these differences through data fusion, the MBEI leverages them to define the uncertainty bounds of the estimates. Consequently, for each 0.1° grid cell, we provide the ensemble mean as the central estimate, while delineating the uncertainty envelope through two metrics: the standard deviation, representing dispersion, and the maximum and minimum bounds, defining the uncertainty range. The overall workflow is illustrated in Fig. 1.

3. As noted by the authors, significant discrepancies exist among different emission inventories. In integrating the bottom-up and top-down approaches in this study, how were the inherent differences between these two methodologies accounted for? Could these uncertainties propagate into the integrated results and consequently affect the accuracy of MBEI?

Response: We appreciate the reviewer’s insightful comment regarding the handling of discrepancies between methodologies and the potential implications for inventory accuracy. We fully concur that significant divergences exist between bottom-up and top-down approaches, as they are predicated on fundamentally distinct physical mechanisms—one relying on post-fire burned area and available fuel loads, and the other on instantaneous radiative energy release. In addressing the reviewer’s concern, we clarify that our framework was deliberately designed not to mathematically eliminate or smooth these inherent differences, but rather to preserve them as a critical diagnostic tool. We posit that in the absence of absolute global ground-truth validation data, force-fitting these divergent methodologies into a single deterministic value often conveys a false sense of precision while obscuring the true epistemic limitations of current observation capabilities.

In the revised manuscript, particularly in the Introduction of Section 2.2, we clarify that our integration strategy is fundamentally designed to preserve, rather than mathematically eliminate, the inherent discrepancies between the two methodologies. As detailed in the newly refined framework

(illustrated in the revised Figure 1 and Table 2), the MBEI operates by generating an ensemble of eight independent sub-inventories—four derived from bottom-up logic (utilizing dynamic AGB and Burned Area as detailed in Eqs. 1–4) and four from top-down logic (utilizing reconstructed diurnal Fire Radiative Energy as detailed in Eqs. 5–13). By running these algorithms in parallel, we treat the divergence between the bottom-up and top-down estimates not as error noise to be smoothed out, but as a direct, quantitative measure of structural uncertainty. Regarding the propagation of these uncertainties into the integrated results, we argue that this propagation is a necessary feature for robust scientific assessment rather than a detriment to accuracy. Given the absence of direct, global-scale ground-truth measurements for fire emissions, a single deterministic estimate often conveys a false sense of precision. Therefore, our methodology focuses on transforming the propagated discrepancies into a quantifiable range. As articulated in our revised methodology, by rigorously quantifying this propagation via ensemble statistics (Mean, Std, Max, Min), the MBEI provides a "uncertainty range." The ensemble mean serves as the central estimate, while the standard deviation and the Min-Max bounds delineate the scope of dispersion among the sub-inventories. This ensures that the final MBEI is not defined by a potentially biased single point, but effectively characterizes the structural variability inherent in the diverse input data and algorithms.

We have comprehensively revised the introductory text of Section 2.2 and the discussion in Section 4.1 to articulate this philosophy clearly. The revised manuscript now explicitly describes this ensemble framework as a system designed to capture and quantify, rather than obscure, the structural uncertainties stemming from algorithm choice. Furthermore, our analysis in Section 4.1 demonstrates that this preserved uncertainty reveals significant spatial heterogeneity—highlighting that discrepancies are driven by specific regional fire regimes (e.g., intense megafires in Australia vs. small fragmented fires in the Middle East)—thereby providing valuable insights into the limitations of current remote sensing techniques across different biomes.

Please refer to Page 10, Lines 243-252 and the following is the revised manuscript:

To quantify global biomass burning emissions and their associated uncertainties, we constructed the MBEI using a multi-source ensemble framework. Unlike conventional approaches that rely on a single algorithm, this framework operates by generating an ensemble of eight independent sub-inventories (see Table 2). This design is explicitly structured to capture the structural uncertainty

stemming from the fundamental mechanistic discrepancies between bottom-up (burned area-based) and top-down (fire radiative power-based) methodologies. Rather than obscuring these differences through data fusion, the MBEI leverages them to define the uncertainty bounds of the estimates. Consequently, for each 0.1° grid cell, we provide the ensemble mean as the central estimate, while delineating the uncertainty envelope through two metrics: the standard deviation, representing dispersion, and the maximum and minimum bounds, defining the uncertainty range. The overall workflow is illustrated in Fig. 1.

Please refer to Fig. 1 and Table 2:

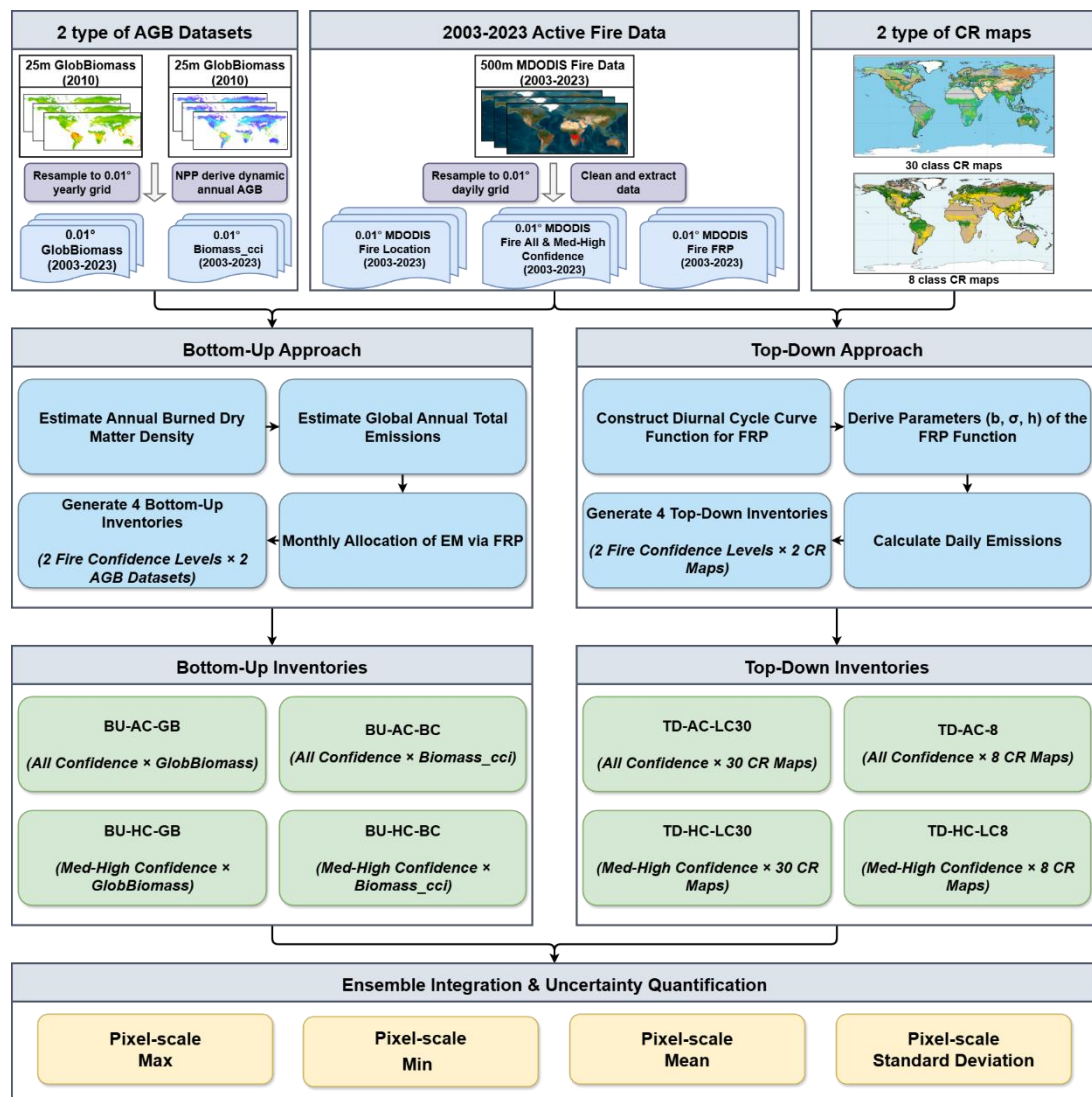


Figure 1. Framework for the construction of MBEI.

Table 2. The detail of the eight biomass burning emission sub-inventories.

4 Bottom-Up Inventories			4 Top-Down Inventories		
Name	Confidence Level	Datasets	Name	Confidence Level	Datasets
BU-AC-GB	All Confidence	GlobBiomass	TD-AC-LC30	All Confidence	30-class CR map
BU-AC-BC	All Confidence	Biomass_cci	TD-AC-LC8	All Confidence	8-class CR map
BU-HC-GB	Medium-to-High confidence	GlobBiomass	TD-HC-LC30	Medium-to-High confidence	30-class CR map
BU-HC-BC	Medium-to-High confidence	Biomass_cci	TD-HC-LC8	Medium-to-High confidence	8-class CR map

Note: The final MBEI dataset also includes the pixel-level ensemble statistics (Mean, Std, Max, Min) calculated from these eight sub-inventories.

4. A detailed explanation should be provided on how the uncertainty in global biomass burning emissions is quantified.

Response: We appreciate the reviewer’s constructive suggestion regarding the need for a more explicit detailed explanation of our uncertainty quantification methodology. We recognize that a transparent description of how variability is mathematically derived is essential for users to properly interpret the inventory’s reliability. Accordingly, we have thoroughly revised Section 2.2 to provide a step-by-step description of the statistical procedures employed to define the uncertainty bounds of the MBEI.

In the revised manuscript, we clarify that the quantification of uncertainty is strictly based on the ensemble spread of the eight independent sub-inventories described in our methodology. The process begins with the rigorous spatial and temporal alignment of these sub-inventories—generated from the parallel execution of bottom-up (varied by AGB datasets and fire confidence) and top-down (varied by biome-specific conversion factors and fire confidence) algorithms—onto a standardized $0.1^\circ \times 0.1^\circ$ monthly grid. Once aligned, we treat the emission estimates from these eight distinct pathways within each grid cell as a statistical ensemble sample. This approach allows us to transform the discrepancies arising from different input data and algorithm logic into quantitative metrics.

To represent this uncertainty mathematically, we calculate a suite of descriptive statistics for every pixel. The ensemble mean is computed to serve as the central estimate of the inventory, integrating the diverse information from all available data streams. By rigorously quantifying this propagation via ensemble statistics (Mean, Std, Max, Min), the MBEI provides a "uncertainty range." Specifically, the standard deviation is calculated to represent the dispersion intensity among the different methods, effectively highlighting regions where algorithm disagreement is high. Concurrently, the maximum and minimum values among the eight estimates are identified to delineate the upper and lower boundaries of the uncertainty envelope. This definition ensures that the reported uncertainty is not an arbitrary error bar, but a physically meaningful range that reflects the current state of knowledge and the limitations inherent in global biomass burning observation. We have updated the text to explicitly detail this calculation workflow, ensuring that the derivation of the "uncertainty range" is clear and reproducible.

Please refer to Page 10, Lines 243-252 and the following is the revised manuscript:

To quantify global biomass burning emissions and their associated uncertainties, we constructed the MBEI using a multi-source ensemble framework. Unlike conventional approaches that rely on a single algorithm, this framework operates by generating an ensemble of eight independent sub-inventories (see Table 2). This design is explicitly structured to capture the structural uncertainty stemming from the fundamental mechanistic discrepancies between bottom-up (burned area-based) and top-down (fire radiative power-based) methodologies. Rather than obscuring these differences through data fusion, the MBEI leverages them to define the uncertainty bounds of the estimates. Consequently, for each 0.1° grid cell, we provide the ensemble mean as the central estimate, while delineating the uncertainty envelope through two metrics: the standard deviation, representing dispersion, and the maximum and minimum bounds, defining the uncertainty range. The overall workflow is illustrated in Fig. 1.

The Revised Manuscript with Changes Highlighted:

The newly developed Multi-ensemble Biomass-burning Emissions Inventory (MBEI): Characterizing and unraveling spatiotemporal uncertainty in global biomass burning emissions

Xinlu Liu^{1,2}, Zhongyi Sun^{2*}, Chong Shi¹, Peng Wang³, Tangzhe Nie⁴, Qingnan Chu⁵, Huazhe Shang¹, Lu Sun⁶, Dabin Ji¹, Meng Guo⁷, Kunpeng Yi⁸, Zhenghong Tan⁹, Lan Wu², Xinchun Lu^{1,4}, Shuai Yin^{1*}

¹State Key Laboratory of Remote Sensing and Digital Earth, Aerospace Information Research Institute, Chinese Academy of Sciences, Beijing 100101, China

²College of Ecology and Environment, Hainan University, Haikou 570228, China

³Department of Atmospheric and Oceanic Sciences, Fudan University, Shanghai, 200438, China

⁴School of Water Conservancy and Electric Power, Heilongjiang University, Harbin 150006, China

⁵Centro de Biotecnología y Genómica de Planta (UPM-INIA). Universidad Politécnica de Madrid, Campus de Montegancedo, Madrid, Spain

⁶School of Human Settlements and Civil Engineering, Xi'an Jiaotong University, Shaanxi Province, 710049, China

⁷School of Geographical Sciences, Northeast Normal University, Changchun 130024, China

⁸State Key Laboratory of Urban and Regional Ecology, Research Center for Eco-Environmental Sciences, Chinese Academy of Sciences, Beijing 100085, China

⁹School of Ecology and Environmental Science, Yunnan University, Kunming 650500, China

Correspondence to: Shuai Yin (yinshuai@aircas.ac.cn) and Zhongyi Sun (gis.rs@hainanu.edu.cn)

Abstract. Large discrepancies among existing inventories hinder a consensus on the true magnitude and long-term trends of global biomass burning emissions. To address this, we developed the Multi-ensemble Biomass-burning Emissions Inventory (MBEI), a framework integrating bottom-up and top-down approaches with multi-source data to generate eight sub-inventories for the period 2003–2023. This ensemble approach allows for the explicit quantification of emission uncertainty at a 0.1° grid scale. We estimate global annual CO₂ emissions at 7304 (4400–9657) Tg, with the maximum estimate exceeding the minimum by over two-fold. The uncertainty exhibits significant spatial heterogeneity: it is highest in low-emission regions like Australia and the Middle East (6.0–7.0 fold difference), whereas traditional hotspots like Africa show lower divergence (Approximately 2 fold). Temporally, a distinct decadal shift was identified: global emissions declined from 2003 to 2013 due to reduced tropical burning, but reversed to an increasing trend from 2013 to 2023, driven by intensified fires in northern high-latitudes and extreme events. Comparisons confirm that the MBEI mean provides a robust central estimate, while its max-min range effectively encompasses other major inventories. By providing explicit uncertainty bounds, MBEI enhances the reliability of atmospheric modeling and climate assessments. The dataset is publicly available at <https://doi.org/10.5281/zenodo.18104830> (Liu and Yin, 2025).

1 Introduction

Biomass burning, encompassing forest fires, grassland fires, and the burning of agricultural residues, is a key disturbance in terrestrial ecosystems (Bowman et al., 2020; Jones et al., 2022). It profoundly influences local and global ecological processes and climate systems by releasing large quantities of greenhouse gases (GHGs) and aerosol particles (Bowman et al., 2009; Letu et al., 2023; Pellegrini et al., 2018; Shi et al., 2025; Yin, 2021). Accelerating climate change is driving significant shifts in the spatiotemporal patterns of global biomass burning, affecting its frequency, intensity, and duration. Observational data indicate that the incidence of extreme biomass burning events has increased 2.2-fold in the last two decades (Cunningham et al., 2024; Wang et al., 2023), and climate models project that high-risk areas for global biomass burning will expand by nearly one-third by the end of the 21st century (Senande-Rivera et al., 2022). Notably, while the burned area is shrinking in some traditional high-frequency burning regions (e.g., tropical rainforests) (Andela et al., 2017; Zheng et al., 2021), the fire-prone season is substantially extending. In regions such as southeastern Australia, eastern Siberia, and eastern North America, the length of fire weather season has increased by 27%–94%, significantly prolonging the period during which ecosystems are exposed to fire risk (Jones et al., 2022).

The increase of biomass burning frequency is raising atmospheric concentrations of GHGs, thereby exerting a strong perturbation on Earth's biospheric processes (Andreae, 2019; Andreae and Merlet, 2001; Yin et al., 2025). Between 1997 and 2016, global carbon emissions from biomass burning averaged 2.2 Pg C per year, equivalent to approximately 6% of global fossil fuel CO₂ emissions in 2014 (Friedlingstein et al., 2025; Liu et al., 2024; van der Werf et al., 2017). This increase in GHGs intensifies global warming, creating a feedback loop that is projected to elevate the risk of extreme fire weather by at least 50% in key regions such as western North America, equatorial Africa, Southeast Asia, and Australia by 2080 (Touma et al., 2021). Furthermore, particulate matter (e.g., black carbon, brown carbon, and organic carbon) emitted from biomass burning poses a serious threat to human health (Reid et al., 2005; Zhang et al., 2020). A meta-analysis of 81 studies (1980–2020) (Karanasiou et al., 2021) showed that exposure to PM_{2.5} and PM₁₀ from biomass burning is significantly associated with all-cause mortality, corresponding to a 1.31% (95% CI: 0.71–1.71) and 1.92% (95% CI: 1.19–5.03) increase for every 10 µg m⁻³ rise in PM₁₀ and PM_{2.5}. These effect sizes exceed typical estimates for all-source ambient particulate matter, indicating that biomass burning PM may pose greater health risks than general ambient PM. From

1990 to 2019, PM_{2.5}-related excess mortality in equatorial Asia increased threefold, with approximately 317 thousand of these deaths attributed to high-intensity biomass burning from Indonesian peatlands (Yin, 2023).

Establishing high-precision emission inventories is crucial for assessing the impacts of biomass burning on the global atmospheric environment and public health (Bray et al., 2021; Filonchyk et al., 2024; Ramanathan and Carmichael, 2008). Trace gases and aerosols released by biomass burning not only affect global climate but also alter regional atmospheric chemistry via transboundary transport (Andreae, 2019). Atmospheric Chemistry Transport Models, which are used for air quality forecasting and source apportionment, rely on emission inventories with high spatiotemporal resolution and reliability. Such data are crucial for accurately resolving pollutant transport and transformation pathways, as well as for quantifying their contributions to pollution (Matthias et al., 2018; Wang et al., 2014). Currently, the construction of global and regional biomass burning emission inventories primarily relies on two established estimation pathways, the bottom-up and top-down approach. The bottom-up approach typically estimates emissions based on satellite-derived burned area (e.g., MODIS MCD64A1) combined with fuel load, combustion completeness, and emission factors (van der Werf et al., 2017; Wiedinmyer et al., 2023). The typical inventories of this approach include the Global Fire Emissions Database (GFED) and the Fire INventory from NCAR (FINN) (Giglio et al., 2006). In contrast, the alternative top-down approach estimates emissions based on Fire Radiative Power (FRP) retrieved from satellites in thermal infrared bands. This method utilizes the relationship between the time-integrated FRP, known as Fire Radiative Energy (FRE), and the total dry matter consumed, a relationship often calibrated using field observations (Ichoku and Ellison, 2014; Wooster et al., 2005). It estimates emissions by fitting the combustion curve of dry matter consumption derived from satellite-retrieved FRP (Santoro, 2018). The typical inventories include the Global Fire Assimilation System (GFAS) and the Quick Fire Emissions Dataset (QFED) (Andela et al., 2015; Giglio et al., 2020).

Although these two methods provide clear theoretical frameworks, their practical implementation varies among researchers in their choice of data sources, parameters, and algorithmic details, leading to significant discrepancies in the resulting inventories (Hoelzemann et al., 2004; Ichoku and Kaufman, 2005; Ito and Penner, 2004; Zhang et al., 2014). Consequently, estimates of total emissions for the same region or period can differ considerably (N'Datchoh et al., 2025; Pereira et al., 2016; Shi and Matsunaga, 2017; Whitburn et al., 2015). This discrepancy poses a key challenge in the field, as it not only directly

impacts the accuracy of atmospheric chemistry simulations and climate effect assessments (Liu et al., 2020; Longo et al., 2010; Stroppiana et al., 2010; Williams et al., 2012) but also leads to a lack of clear consensus on the true magnitude and long-term trends of global biomass burning emissions.

A growing body of evidence suggests that under the dual threats of climate change and human activities, the spatial distribution of global biomass burning is undergoing significant shifts. Fire activity is weakening in some traditional tropical hotspots (e.g., African savannas) while intensifying in high-latitude boreal forests (Tyukavina et al., 2022; van Wees et al., 2021; Yin et al., 2020b; Zheng et al., 2021, 2023). These complex and opposing regional trends obscure the long-term trajectory of global total emissions. In this context, the limitation of emission inventories, which provide only a single estimate, becomes more prominent. A single value cannot capture the extent to which observed regional trends reflect genuine physical processes versus mere algorithmic artifacts of a particular inventory. Therefore, accurately assessing the current state of biomass burning emissions requires not only improving the precision of inventories but also developing new methods to systematically quantify their uncertainty.

To address this challenge, we constructed the Multi-ensemble Biomass-burning Emissions Inventory (MBEI), a global biomass burning emission dataset for 2003–2023, by integrating mainstream top-down and bottom-up algorithms. This ensemble approach incorporates two fire-detection products and four sets of key input variables, resulting in eight distinct sub-inventories that quantify emissions for 11 key species (e.g., CO₂, PM_{2.5}, BC, and NO₂). By analyzing the mean and the maximum-minimum range (hereafter referred to as the "Max-Min band") of these eight sub-inventories, our study provides a new quantitative estimate of global biomass burning emissions over the past 21 years and, crucially, reveals their uncertainty across various spatial scales. It offers quantitative evidence to better interpret the shifts in global biomass burning patterns. The advantages of this new inventory allow data users (such as atmospheric chemistry modelers and climate assessment experts) to directly incorporate the variability of emission estimates into their analytical frameworks, thereby providing critical data support for dissecting complex global biomass burning dynamics and enhancing the robustness of their assessment results.

2 Materials and Methods

2.1 Datasets

The MBEI integrates two established methodologies: a bottom-up approach based on burned area and a top-down approach based on FRP (Vermote et al., 2009; Wiedinmyer et al., 2006). Active fire detections were sourced from the MODIS Near-Real-Time product (MCD14DL). To assess uncertainty stemming from detection confidence, we created two parallel processing streams using fire pixels from both Aqua and Terra satellites (2003–2023): one including all detected fires, and another restricted to fires with medium-to-high confidence (>30%). In addition, we introduced combination in key input variables: the bottom-up algorithm was driven by two alternative aboveground biomass (AGB) datasets (Biomass_cci and GlobBiomass), while the top-down algorithm utilized two different biome maps (8-class and 30-class) to define emission coefficients. For consistency, all input datasets were resampled to a common 0.1° spatial resolution and monthly temporal resolution. A comprehensive list of the datasets used in this study is provided in Table 1.

Table 1. Datasets used in this study.

Data types	Name	Temporal Coverage	Spatial Resolution	Temporal Resolution	Reference
Active Fire Data	Aqua MCD14DL	2003-2023	1 km × 1 km	daily	(NASA VIIRS Land Science Team, 2021)
	Terra MCD14DL	2003-2023	1 km × 1 km	daily	(NASA VIIRS Land Science Team, 2021)
Burning Efficiency (BE) & Emission Factor (EF) Data	EF Classification Source Data GFED	\	0.25° × 0.25°	\	(van der Werf et al., 2006)
	EF Coefficients	\	\	\	(van der Werf et al., 2017)
	BE Coefficients	\	\	\	(Shi et al., 2015)
AGB Data	GlobBiomass	2010	25 m × 25 m	\	(Santoro, 2018)
	Biomass_cci	2010/2015-2021	100 m × 100 m	yearly	(Santoro and Cartus, 2024)
Conversion Factor (CR) Data	30-class CR map	\	0.1° × 0.1°	\	(Kaiser et al., 2023)
	8-class CR map	\	0.1° × 0.1°	\	(Kaiser et al., 2012)
Ancillary & Validation Data	Net Primary Production (NPP) MYD17A3HGF v061	2003-2023	500 m × 500 m	yearly	(Running and Zhao, 2021)
	Land Cover Type MCD12Q1.061	2003-2023	500 m × 500 m	yearly	(Friedl and Sulla-Menashe, 2022)
Validation Inventory Data	Global Fire Emissions Database 5 (GFED 5)	2003-2022	0.25° × 0.25°	daily	(Binte Shahid et al., 2024; Vernooij et al., 2023; Wiggins et al., 2021)
	Fire INventory from NCAR 2.5 (FINN 2.5) MODIS	2002-2022	0.1° × 0.1°	daily	(Wiedinmyer et al., 2023)
	Global Fire Assimilation System 1.2 (GFAS 1.2)	2003-2022	0.1° × 0.1°	daily	(Kaiser et al., 2012)
	Quick Fire Emissions Dataset 3.1 (QFED 3.1)	2003-2022	0.1° × 0.1°	daily	(Koster et al., 2015)

Note: The 8-class biome map is derived from the 30-class biome map. See [Fig. S1](#) for its spatial distribution.

2.1.1 Active fire detection and fire radiative power

The sourced active fire data were obtained from the MODIS Near-Real-Time active fire product (MCD14DL C6.1), provided by NASA's Fire Information for Resource Management System (FIRMS). This product provides fire detections from both the Terra and Aqua satellites based on the MOD14/MYD14 thermal anomalies algorithm (Giglio et al., 2006). Each active fire detection represents the center of a 1-km pixel flagged as containing one or more fires.

For the period 2003–2023, we extracted daily fire locations, detection confidence, and FRP values. These 1-km daily data were then aggregated into monthly 0.1° grids, which form the primary input for both our top-down and bottom-up frameworks.

2.1.2 Burning efficiency and emission factor

To assign region- and vegetation-specific BE and EF, we first utilized the annual 500-m MODIS Land Cover Type product (MCD12Q1 C6.1), adopting its International Geosphere-Biosphere Programme (IGBP) classification scheme. We then assigned a BE value to each of the 17 IGBP classes using coefficients derived from Mieville et al. (2010) and Shi et al. (2015), with the specific values detailed in [Table S3](#).

Emission factors were assigned by intersecting the MCD12Q1 land cover map with the 14 continental-scale regions defined by GFED (van der Werf et al., 2017). This process yielded a unique EF for each landcover region combination, allowing us to estimate emissions for 11 key atmospheric emission species as detailed in [Table S4](#).

2.1.3 Aboveground biomass

To quantify available fuel load for the bottom-up framework and assess related uncertainties, we employed two independent global AGB datasets. The GlobBiomass provides a global AGB map at 25-m spatial resolution for the baseline year 2010, generated by synergistically fusing multi-source data, including observations from spaceborne Synthetic Aperture Radar (SAR), Light Detection and Ranging (LiDAR), and optical remote sensing, together with forest inventory data (Santoro, 2018). Biomass_cci, provided by the European Space Agency Climate Change Initiative (ESA CCI) project, contains global AGB maps at 100-m resolution for multiple years (2010, 2017, 2018, and annually for 2019–2021) (Mariani et al., 2016).

2.1.4 Conversion factor

In the top-down method, satellite-derived FRE, which is the temporal integral of FRP, is converted into the mass of combusted dry matter. This conversion is performed using a biome-specific conversion factor (kg Dry Matter MJ⁻¹). To assess the uncertainty associated with this parameter, we implemented two distinct sets of conversion factors: one based on the 8 major biomes used in the GFAS (Kaiser et al., 2012), and another based on a more detailed 30-class biome map. The spatial distributions and respective CR values for these two schemes are detailed in [Figs. S1–S2 and Tables S1–S2](#).

2.1.5 Ancillary and validation data

To derive a dynamic annual AGB time series for 2003–2022 from otherwise static AGB maps, we used the MODIS annual Net Primary Production product MYD17A3HGF v061, which provides global NPP at 500 m spatial resolution. We leveraged the empirically supported linear relationship between NPP and AGB to temporally extrapolate the baseline AGB maps and generate annual AGB maps, with the detailed procedure and parameterization described in Section 2.2.1.

To evaluate the performance and robustness of the new inventory, we conducted a comprehensive intercomparison with four widely used global emission products that span both bottom-up and FRP methodologies. For the bottom-up approach, GFED 5.0 serves as a key benchmark, as its reliance on the Carnegie–Ames–Stanford Approach (CASA) biogeochemical model for fuel load estimation allows for a critical assessment of how a model-driven workflow differs from our use of direct remotely sensed AGB. To specifically isolate the influence of parameter choices (e.g., emission factors and burning efficiency), we included FINN 2.5 in our analysis. Because it is built upon the same MODIS active fire and land cover inputs, a comparison with FINN 2.5 provides a controlled setting to evaluate the impact of our system's unique parameterization. For the top-down FRP-based approach, GFAS 1.2 provides a reference for evaluating the plausibility of the combustion-rate coefficient schemes tested in this study, as it converts satellite-observed FRP to dry matter combusted in a manner consistent with our framework. Finally, we incorporated QFED 3.1, which represents an optimized evolution of GFAS applying more advanced correction and gap-filling procedures, to examine how alternative imputation strategies for missing FRP retrievals affect the spatiotemporal completeness of the final emission estimates.

2.2 The framework for the MBEI

To quantify global biomass burning emissions and their associated uncertainties, we constructed the MBEI using a multi-source ensemble framework. Unlike conventional approaches that rely on a single algorithm, this framework operates by generating an ensemble of eight independent sub-inventories (see Table 2). This design is explicitly structured to capture the structural uncertainty stemming from the fundamental mechanistic discrepancies between bottom-up (burned area-based) and top-down (fire radiative power-based) methodologies. Rather than obscuring these differences through data fusion, the MBEI leverages them to define the uncertainty bounds of the estimates. Consequently, for each 0.1° grid cell, we provide the ensemble mean as the central estimate, while delineating the uncertainty envelope through two metrics: the standard deviation, representing dispersion, and the maximum and minimum bounds, defining the uncertainty range. The overall workflow is illustrated in Fig. 1.

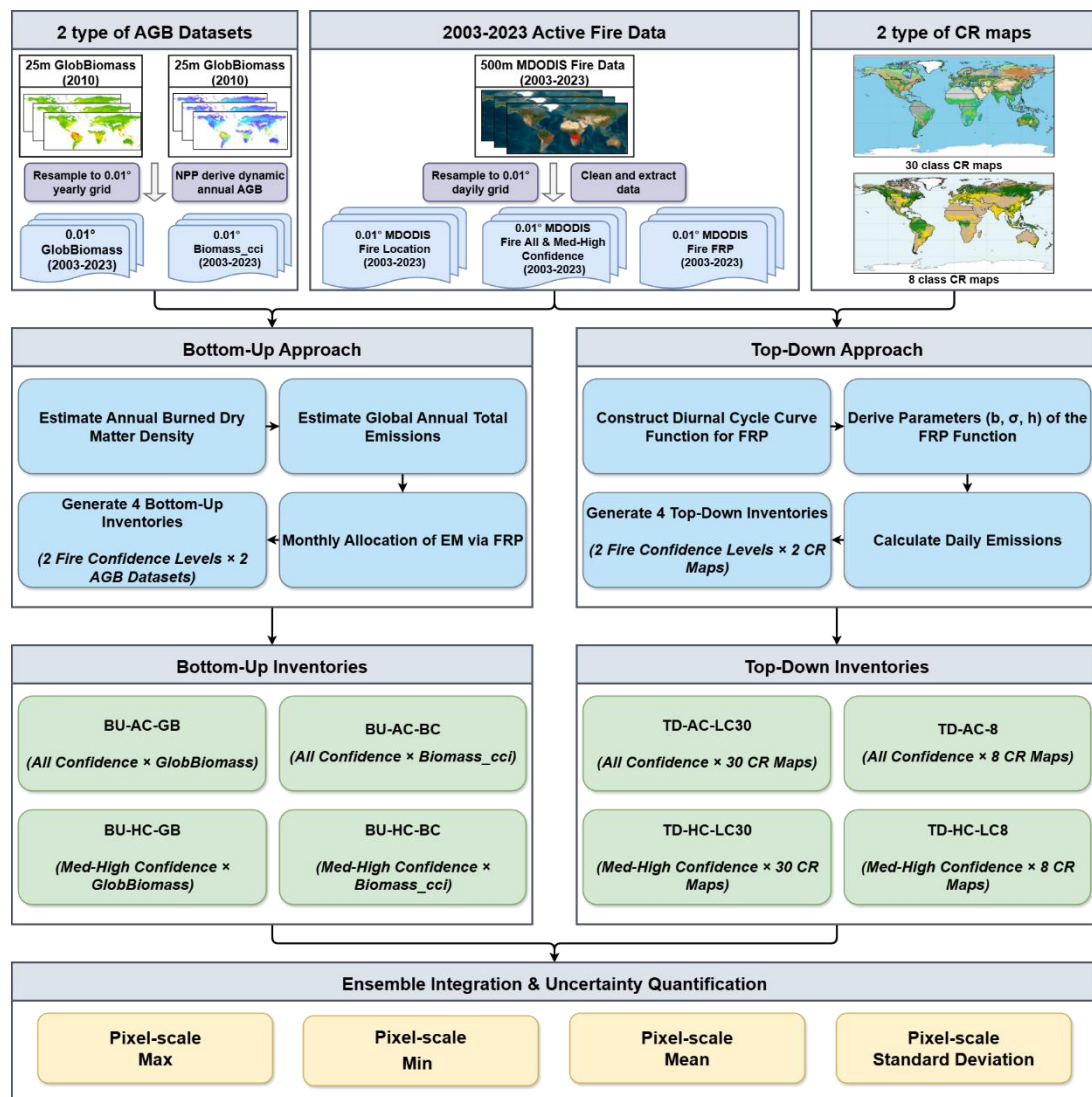


Figure 1. Framework for the construction of MBEI.

Table 2. The details of the eight biomass burning emission sub-inventories.

4 Bottom-Up Inventories			4 Top-Down Inventories		
Name	Confidence Level	Datasets	Name	Confidence Level	Datasets
BU-AC-GB	All Confidence	GlobBiomass	TD-AC-LC30	All Confidence	30-class CR map
BU-AC-BC	All Confidence	Biomass_cci	TD-AC-LC8	All Confidence	8-class CR map
BU-HC-GB	Medium-to-High confidence	GlobBiomass	TD-HC-LC30	Medium-to-High confidence	30-class CR map
BU-HC-BC	Medium-to-High confidence	Biomass_cci	TD-HC-LC8	Medium-to-High confidence	8-class CR map

Note: The final MBEI dataset also includes the pixel-level ensemble statistics (Mean, Std, Max, Min) calculated from these eight sub-inventories.

2.2.1 Bottom-up emission estimation

This study employs a bottom-up method, combining multi-source remote sensing data to construct four global monthly biomass burning emission inventories for 2003–2023. The core computational workflow involves four key steps: (1) constructing a dynamic annual AGB dataset based on interannual variations in NPP; (2) modeling the total burned dry matter density (BD) under multiple fire events within a year; (3) estimating total annual emissions (EM) by burned area (BA), BD and EF; (4) downscaling annual emissions to a monthly resolution using the monthly distribution of FRP.

To overcome the limitation of using a static AGB benchmark map that ignores interannual variability, we constructed a dynamic annual AGB dataset. Based on the ecological assumption of a stable proportional relationship between AGB and NPP (Raich et al., 2006; Whittaker and Likens, 1972), we used the relative interannual changes in the MODIS annual NPP product to extrapolate the baseline AGB. The AGB for a target year (m) in a specific pixel (p) is calculated as:

$$AGB_{(m,p)} = AGB_{(a,p)} \times \frac{NPP_{(m,p)}}{NPP_{(a,p)}} \quad (1)$$

where $AGB_{(m,p)}$ is the AGB in year m at pixel p ($Mg\ ha^{-1}$); $AGB_{(a,p)}$ is the baseline AGB at pixel p (mean of 2003–2023, $Mg\ ha^{-1}$); $NPP_{(m,p)}$ is the NPP in year m at pixel p ($kg\ C\ m^{-2}\ yr^{-1}$); and $NPP_{(a,p)}$ is the baseline mean NPP at pixel p ($kg\ C\ m^{-2}\ yr^{-1}$).

After obtaining annual AGB, we estimated the annual BD per unit area. Considering that a pixel may experience multiple fires in a year, we used the following model to simulate the sequential consumption of AGB by fire and accumulate the total annual burned amount:

$$BD_{(m,p)} = \sum_{j=1}^I \{AGB_{(m,p)} \times (1-BE_c)^{j-1} \times BE_c\} \quad (2)$$

where $BD_{(m,p)}$ is the total burned dry matter density in year m at pixel p (kg m^{-2}); I is the fire frequency in year m at pixel p (derived from active fire data); j represents the j -th fire event of the year; $AGB_{(m,p)}$ is the initial AGB at the beginning of the year (kg m^{-2}); and BE_c is the dimensionless burning efficiency for the land cover type c of pixel p (derived from the Land Cover Type MCD12Q1.061).

The total annual emissions of each pollutant are estimated based on the method proposed by Seiler and Crutzen (1980):

$$EM_{(m,p)} = BA_{(m,p)} \times BD_{(m,p)} \times EF \quad (3)$$

where $EM_{(m,p)}$ is the annual emission of a specific pollutant in year m at pixel p (g); $BA_{(m,p)}$ is the total annual burned area in year m at pixel p (m^2), obtained by multiplying the annual MODIS active fire location mask by the pixel's geographic area to ensure that the burned location is consistent with fire detections; $BD_{(m,p)}$ is the annual burned dry matter density (kg m^{-2}) calculated from Eq. (2); and EF is the emission factor for the specific pollutant (g kg^{-1}). It is important to note that inputs with annual temporal resolution (e.g., AGB, Land Cover-derived BE and EF) determine the magnitude of $EM_{(m,p)}$ in this step and are not interpolated.

Finally, to obtain a monthly-resolution emission inventory, we applied a temporal allocation approach. We used satellite-observed FRP as a high-frequency proxy for fire activity intensity to distribute the total annual emissions $EM_{(m,p)}$ into each month (t):

$$EM_{(m,p,t)} = EM_{(m,p)} \times \frac{FRP_{(m,p,t)}}{\sum_{t=1}^{12} FRP_{(m,p,t)}} \quad (4)$$

where $EM_{(m,p,t)}$ is the pollutant emission in month t of year m at pixel p (g); and $FRP_{(m,p,t)}$ is the monthly cumulative FRP in month t of year m at pixel p (MJ s^{-1}). This method ensures that while the total emission magnitude is constrained by annual fuel loads, the seasonality is driven by real-time fire radiative observations.

2.2.2 Top-down emission estimation

Our top-down emission estimation is based on the FRP approach, which uses satellite-observed thermal radiation to quantify biomass burning. The entire computational framework revolves around FRE, with the final pollutant emissions calculated as:

$$EM_{(p)} = FRE_{(p)} \times CR_{(r)} \times EF \quad (5)$$

where $EM_{(p)}$ is the daily emission at pixel p (g); $FRE_{(p)}$ is the daily cumulative FRE at pixel p (MJ); $CR_{(r)}$ is the conversion factor for the biome r where pixel p is located (kg Dry Matter MJ⁻¹); and EF is the emission factor for the specific pollutant (g kg⁻¹).

However, polar-orbiting satellites like MODIS provide only limited observations per day, making it impossible to obtain daily cumulative FRE by simple integration of instantaneous FRP. To overcome this, we reconstruct the FRP diurnal cycle by fitting a Gaussian function, following the methodology of Vermote et al. (2009). We assume that the diurnal variation of FRP for a single biomass burning event can be represented by a Gaussian function:

$$FRE_{(p)} = \int_0^{24} FRP(t)_{(p)} dt = \int_0^{24} FRP_{\text{peak}(p)} \left(b + c \frac{(t-h)^2}{2\sigma^2} \right) dt \quad (6)$$

where $FRP(t)_{(p)}$ is the instantaneous FRP at local time t for pixel p ; $FRP_{\text{peak}(p)}$ is the peak FRP of the fire event at pixel p (MJ s⁻¹); h is the local time of peak FRP hours; σ is the standard deviation of the Gaussian function, characterizing energy release concentration of the fire; and b is a background term reflecting residual or background radiation during non-active burning periods. The Gaussian parameters b , σ , and h are empirically derived for each biome from the long-term mean FRP ratio between Terra and Aqua observations using the relationships (henceforth $\frac{\overline{FRP}_{\text{Terra}}}{\overline{FRP}_{\text{Aqua}}}$):

$$b = 0.86 \times \left(\frac{\overline{FRP}_{\text{Terra}}}{\overline{FRP}_{\text{Aqua}}} \right)^2 - 0.52 \times \frac{\overline{FRP}_{\text{Terra}}}{\overline{FRP}_{\text{Aqua}}} + 0.08 \quad (7)$$

$$\sigma = 3.89 \times \frac{\overline{FRP}_{\text{Terra}}}{\overline{FRP}_{\text{Aqua}}} + 1.03 \quad (8)$$

$$h = -1.23 \times \frac{\overline{FRP}_{\text{Terra}}}{\overline{FRP}_{\text{Aqua}}} + 14.57 \quad (9)$$

where $\overline{FRP}_{\text{Terra}}$ and $\overline{FRP}_{\text{Aqua}}$ are the long-term mean FRP values for the respective sensors within that biome (MJ s⁻¹).

The final FRP_{peak} is determined by selecting either the daily peak FRP from the Aqua satellite (henceforth $FRP_{Aqua\ peak}$) or the daily peak FRP from the Terra satellite after correction with Eq. (12) (henceforth FRP_{Terra_corr}):

$$FRP_{Aqua\ peak(p)} = \frac{FRP_{Aqua(p)}}{\left(b + e^{-\frac{(1.5-h)^2}{2\sigma^2}}\right) + \left(b + e^{-\frac{(13.5-h)^2}{2\sigma^2}}\right)} \quad (10)$$

$$FRP_{Terra\ peak(p)} = \frac{FRP_{Terra_corr(p)}}{\left(b + e^{-\frac{(1.5-h)^2}{2\sigma^2}}\right) + \left(b + e^{-\frac{(13.5-h)^2}{2\sigma^2}}\right)} \quad (11)$$

$$FRP_{Terra_corr(p)} = FRP_{Terra(p)} \times \frac{\overline{FRP}_{Terra}}{\overline{FRP}_{Aqua}} \quad (12)$$

where $FRP_{Terra_corr(p)}$ is the corrected Terra FRP at pixel p ($MJ\ s^{-1}$), FRP_{peak} was calculated from Aqua satellite data using Eq. (10), following the approach of Vermote et al. (2009). Additionally, FRP values from the Terra satellite were adjusted using Eq. (12). This adjustment utilized long-term FRP ratios for different biomes to normalize the morning Terra observations to the afternoon measurement time of the Aqua satellite.

Independent daily FRE estimates were then calculated using the original Aqua observations ($FRP_{Aqua\ peak(p)}$) and the corrected Terra observations ($FRP_{Terra\ peak(p)}$) in Eq. (6) at pixel p ($MJ\ s^{-1}$). The final daily FRE is the average of these two estimates:

$$FRE_{(p)} = \frac{FRE_{Aqua(p)} + FRE_{Terra(p)}}{2} \quad (13)$$

Through these steps, we obtained the final daily FRE data. We then used Eq. (5) to calculate emissions and aggregated them to a monthly scale, ultimately producing four independent top-down emission inventories.

2.3 Trend analysis

Long-term trends in biomass burning emissions (2003–2022) were quantified using the Theil-Sen median trend estimator, with statistical significance assessed by the Mann-Kendall (MK) test (Mann, 1945; Sen, 1968). This non-parametric approach is particularly suitable for geophysical time series like emission data, as it is robust to outliers and does not assume a normal distribution.

The Theil-Sen estimator calculates the median of the slopes between all pairs of data points in the time series, making it robust to outliers (e.g., emission peaks from extreme fire years) and providing a stable estimate of the long-term trend. The slope is calculated as:

$$\text{slope} = \text{median} \frac{x_j - x_i}{j - i} (1 \leq i < j \leq n) \quad (14)$$

where slope is the estimated trend, x_i and x_j are the data values at time points i and j , and n is the length of the time series.

3 Results

3.1 Spatial patterns and uncertainty of global biomass burning emissions

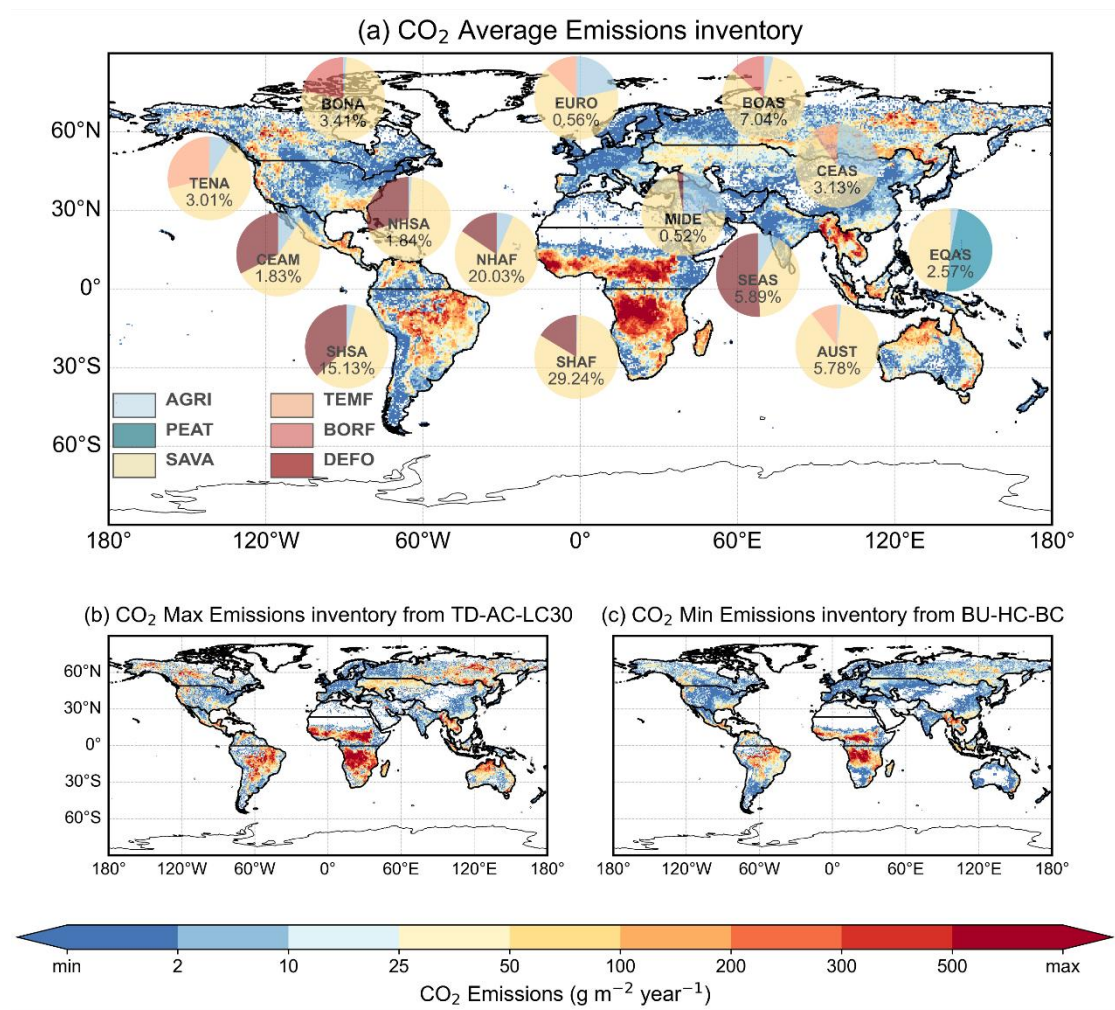


Figure 2. Spatial patterns and regional composition of global biomass burning CO₂ emissions (mean of 2003–2023). (a) Spatial distribution of the annual mean CO₂ emission flux estimated from the mean of the eight inventories in this study. The embedded pie charts show the emission composition for 14 major regions, where: 1) the number in the pie chart indicates the percentage of that region's emissions relative to the global total; and 2) the sectors of the pie chart represent the proportional contribution of six major fire types to the region's total emissions. (b) and (c) show the spatial emission patterns corresponding to the inventory with the highest global total annual emissions (TD-AC-LC30) and the lowest global total annual emissions (BU-HC-BC) among the eight inventories over the entire study period, respectively.

CO₂ is a principal greenhouse gas and the most widely studied species in biomass-burning inventories; accordingly, Sections 3.1–3.4 focus on CO₂, and results for other species are provided in the Supplementary Information. For 2003 to 2023, the framework-mean global annual emissions for all species are summarized in Table 3 and Table S5. The framework-mean CO₂ emission is 7303.63 Tg yr⁻¹, and the associated uncertainty, quantified as the range of annual means across the eight sub-inventories in the ensemble, spans 4400.08 to 9656.89 Tg yr⁻¹.

Fig. 2 shows the highly heterogeneous spatial pattern of mean annual CO₂ emission fluxes (the spatial patterns for other major pollutants are presented in Fig. S6). Global emission activities are largely concentrated in tropical and subtropical regions, characterized by high emission fluxes (> 300 g m⁻² yr⁻¹). Within these areas, the most intense emission hotspots (> 500 g m⁻² yr⁻¹) are clearly identified over the Congo Basin, surrounding savannas, and parts of Southern Africa. This high spatial concentration of intense burning directly translates to Africa's dominant role in the global emission budget. Based on regional statistics (Global 14 regions defined in Fig. S3), Southern Hemisphere South Africa (SHAF) and Northern Hemisphere South Africa (NHAF) collectively contribute 49.2% of global CO₂ emissions (29.2% and 20.0%, respectively). Furthermore, Southern Hemisphere South America (SHSA, 15.1%), Boreal Asia (BOAS, 7.0%), and Southeast Asia (SEAS, 5.9%) also stand out as major source regions for global biomass burning.

The dominant types of biomass burning vary substantially by region (see Fig. S4 for the classification of fire types), leading to distinct emission profiles (see Fig. S5 for the composition of fire types in each region). In the top three emitting regions (SHAF, NHAF, and SHSA), which collectively account for nearly two-thirds (64.4%) of global CO₂ emissions, burning is driven primarily by savanna fires (SAVA) and deforestation fires (DEFO). The contribution of different fire types varies significantly among these top regions (see Fig. 2a for detailed emission values). In SHAF, the largest source, SAVAs are overwhelmingly dominant, accounting for 83% of its CO₂ emissions. A similar pattern occurs in NHAF, where SAVAs contribute 78% of emissions, although agricultural waste burning (AGRI) also plays a notable role (6%). In contrast, the emissions in SHSA are more evenly split between SAVAs (59%) and DEFO fires (37%). In the high-latitude regions of BOAS and Boreal North America (BONA), fires in boreal forests (BORF) are a characteristic emission source, contributing 14% and 22% of regional CO₂ emissions, respectively. Notably, our analysis identifies fires classified as SAVAs as the largest contributor

in both regions (83% in BOAS and 77% in BONA). It is critical to note that SAVA in this context refers to the burning of extensive grasslands and shrublands located within the boreal climate zone, as defined by our underlying land cover dataset, rather than tropical savannas. This highlights that non-forest fires are the dominant source of emissions even in these high-latitude zones.

The emission composition of Equatorial Asia (EQAS) is unique. Although its total emissions are relatively low, it is the only region dominated by peatland fires (PEAT), with PEAT emissions contributing as much as 91.34 Tg yr⁻¹ of CO₂ (48.4% of the regional total). This uniqueness stems from its specific fire regime: vast areas of organic-rich peatlands become highly flammable after being drained and converted to agricultural land (e.g., oil palm plantations). Such fires often manifest as long-duration, hard-to-extinguish subsurface smoldering, leading to extremely high carbon emission intensities and making EQAS a unique and closely watched case in global biomass burning research.

The spatial heterogeneity of this uncertainty is illustrated in Figs. 2b and 2c, which map the highest and lowest emission estimates across the ensemble. Globally, the uncertainty is substantial, with the maximum estimate of annual CO₂ emissions being 2.2 times higher than the minimum estimate across the MBEI sub-inventories.

Importantly, **high biomass** burning emission uncertainty is not found in traditional biomass burning hotspots. Instead, some of the highest uncertainties are found in regions with lower overall emissions. Specifically, Australia and New Zealand (AUST) and the Middle East (MIDE) exhibit the greatest uncertainty, with maximum-to-minimum (max/min) emission ratios reaching 7.18 and 6.40, respectively. In AUST, this extreme uncertainty is linked to its fire regime dominated by highly intermittent and catastrophic megafires (e.g., the 2019–2020 events), which pose significant challenges to consistent estimation across different algorithms. In MIDE, which contributes only 0.52% to the global total, the high uncertainty stems from small, scattered AGRI and SAVA. These weak fire signals are near the lower limit of satellite detection capabilities, a fact confirmed by the large discrepancy observed when comparing estimates derived from 'all confidence' versus 'high and medium confidence' active fire data. In contrast, the major tropical burning regions show much lower relative uncertainty, despite their massive contribution to global emissions. The African (SHAF, NHAF) and South American (SHSA) hotspots have max/min ratios consistently below 2.0. This greater consensus among methods is attributable to the nature of their fires: large-scale, intense, and seasonally predictable SAVA that are robustly captured by various estimation approaches. Meanwhile, temperate and high-latitude regions

such as Central Asia (CEAS), BONA, and Europe (EURO) show intermediate levels of uncertainty, with max/min ratios between 3.5 and 4.0.

In summary, this analysis reveals a critical divergence between the spatial patterns of emission magnitudes and their estimation uncertainties. While emission hotspots are concentrated in tropical regions dominated by regular SAVA and DEFO, the highest uncertainties occur in areas characterized by either highly intermittent megafires (e.g., AUST) or weak, scattered burning (e.g., MIDE), posing distinct challenges to current estimation methods.

Table 3. Total annual CO₂ emissions (Maximum, Minimum, and Average, unit: Tg) for 2003–2023.

Year	Maximum	Minimum	Average	Year	Maximum	Minimum	Average
2003	10882.90	4487.65	7673.68	2014	9258.62	4489.87	7265.29
2004	10842.08	4271.50	7522.16	2015	9688.74	5035.46	7701.46
2005	10391.58	4350.62	7328.15	2016	8476.61	4059.68	6789.30
2006	9663.37	4160.83	7077.83	2017	9250.64	4436.15	7042.77
2007	11063.35	4641.22	7751.48	2018	8727.34	4160.93	6911.22
2008	9725.05	4030.68	6925.95	2019	9747.60	4971.22	7657.46
2009	8661.02	3930.36	6669.83	2020	9295.62	4375.98	7249.50
2010	10253.23	4748.50	7554.59	2021	10696.69	4767.44	7705.11
2011	9653.73	4119.74	7205.26	2022	7289.55	3348.45	6442.83
2012	10537.30	4721.32	7895.63	2023	10527.88	5206.72	8506.96
2013	8161.82	4087.36	6489.87	Mean	9656.89	4400.08	7303.16

3.2 Seasonality of biomass burning emissions

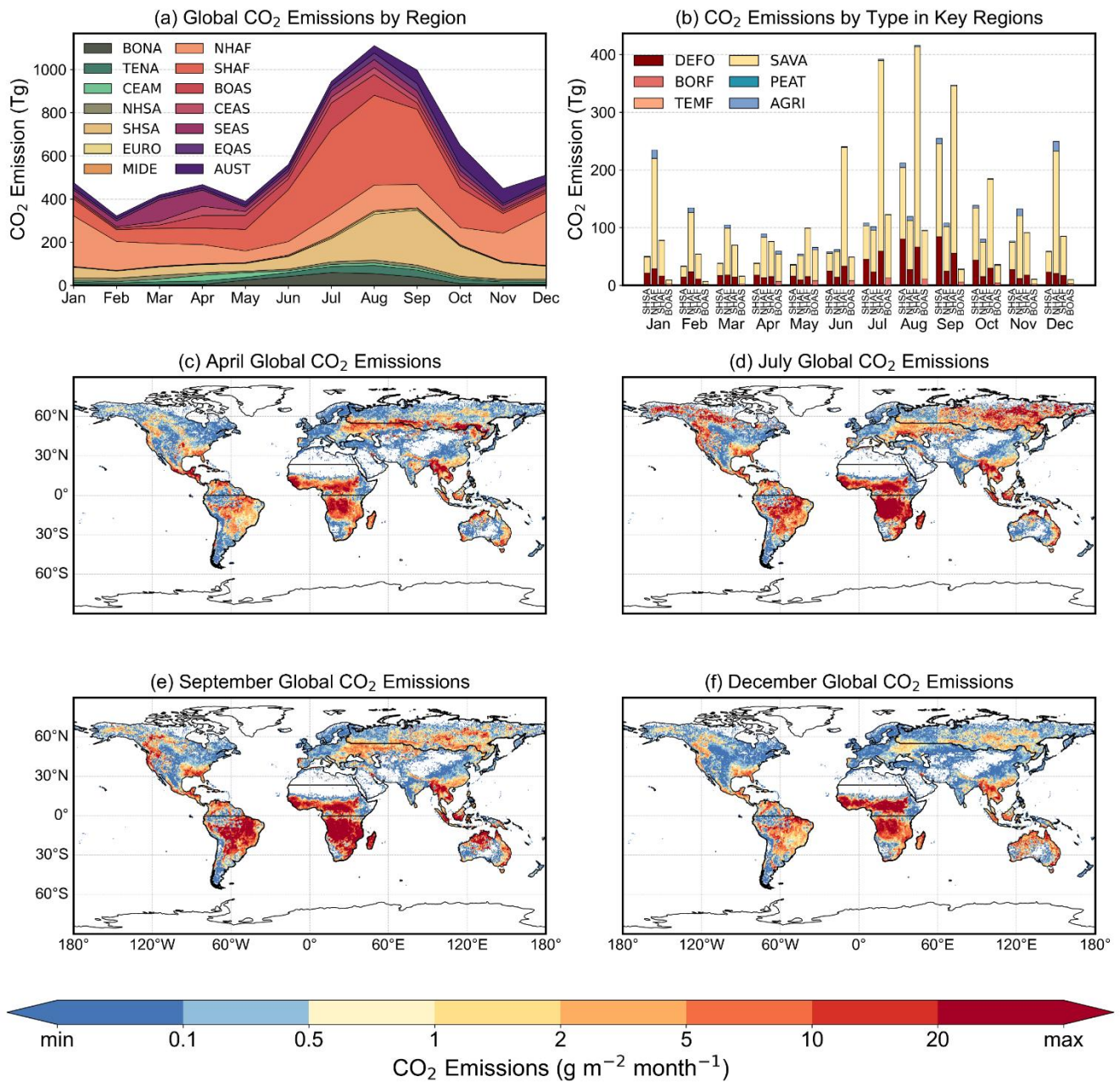


Figure 3. Seasonal cycle and spatial dynamics of global biomass burning CO₂ emissions (mean of 2003–2023). (a) Global monthly emissions partitioned by source region. (b) Monthly emissions for the four primary contributing regions, showing the composition by fire type. (c–f) Spatial distribution of mean monthly emission flux during key seasonal phases: April, July, September, and December.

The MBEI 2003–2023 CO₂ emission inventory reveals a distinct bimodal seasonal cycle (Fig. 3a). Global emissions reach a minimum in February and then climb to a primary peak in the Northern Hemisphere's late summer (August–September). This global pattern results from the combined effect of staggered fire seasons in key regions. Four regions in particular (SHAF, NHA, SHSA, and BOAS) drive this cycle,

collectively accounting for over 71% of total annual emissions (Fig. 3b). For a detailed view of the emission sources, Fig. S7 shows the monthly composition of CO₂ emissions by the six fire types for each of the 14 global regions during 2003–2023.

The annual cycle begins its ascent after the global minimum in February, initially driven by fire activity in the Northern Hemisphere. Persistent dry-season burning in NHAF transitions into an intensifying fire season across Eurasia. By April, the focus of burning activity clearly shifts northward, with emissions surging in regions like BOAS, while the major Southern Hemisphere burning regions (SHAF and SHSA) remain in a period of low activity (Fig. 3c).

From May onwards, global emissions accelerate rapidly, driven by the increasing overlap of fire seasons in both hemispheres. While boreal fires in regions like BOAS reach their annual peak in July, the dominant driver of this global surge is the explosive onset of the fire season in SHAF. Concurrently, burning intensifies in SHSA, and this synergistic effect pushes global emissions towards their annual maximum (Fig. 3d).

The global emission peak in August and September is dominated by the Southern Hemisphere, as fire activity wanes in the major Northern Hemisphere regions. During this period, burning in SHSA reaches its annual zenith, fueled by a combination of DEFO and SAVA. Although past its own peak, SHAF remains the single largest regional contributor to global emissions (Fig. 3e).

Beginning in October, the onset of the rainy season in the Southern Hemisphere rapidly suppresses fire activity there, causing a sharp decline in global emissions. This marks a decisive shift in the global burning pattern. The focus of activity returns entirely to NHAF, which enters its primary fire season that lasts through the subsequent winter (Fig. 3f). This distinct hemispheric seesaw effect completes the annual cycle. Fig. S8 presents the spatial distribution patterns of monthly CO₂ emissions from global biomass burning during the period 2003–2023.

3.3 Interannual variability and long-term trends

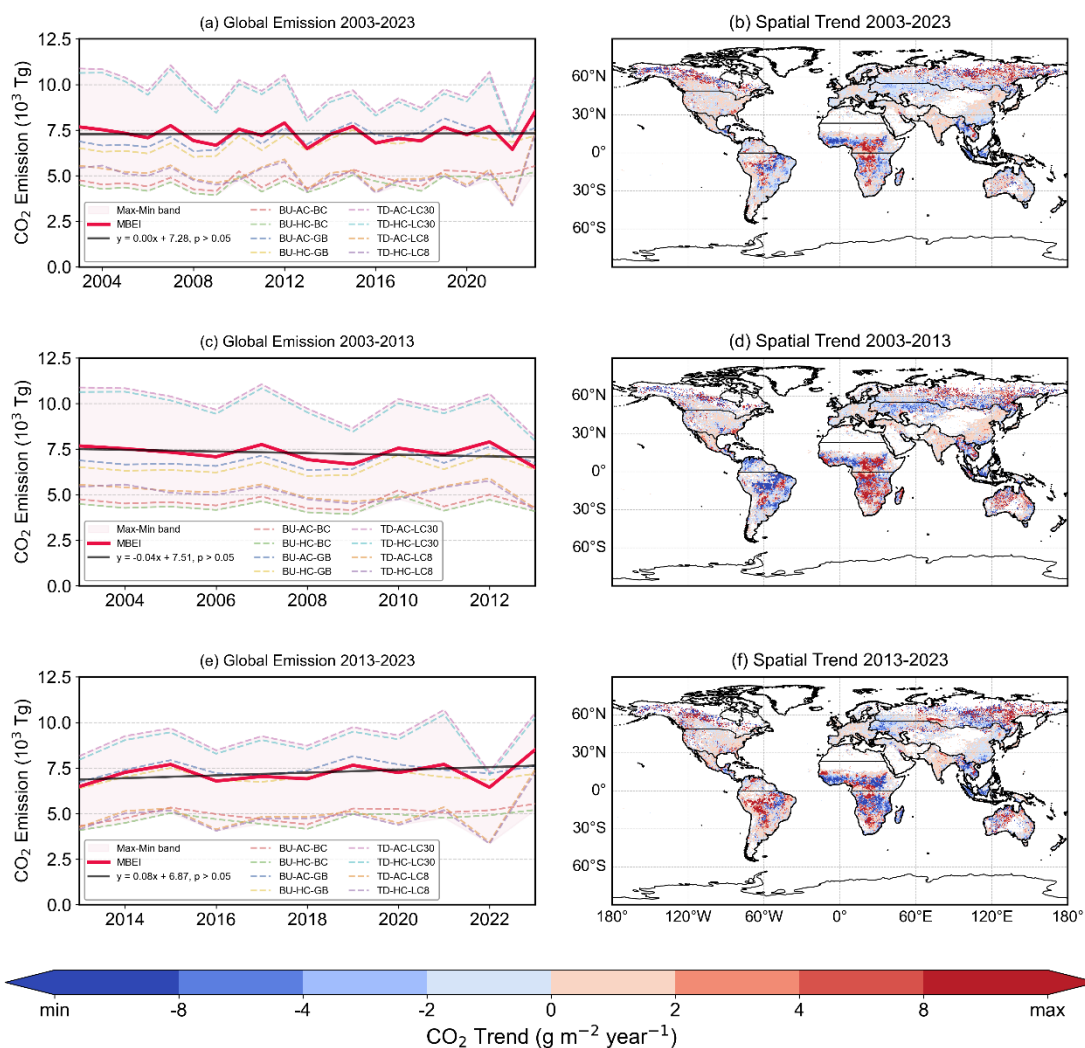


Figure 4. Temporal and spatial trends of global biomass burning CO₂ emissions from 2003 to 2023. (a, c, e) Interannual variation of total emissions and (b, d, f) trends in emission flux for three periods: 2003–2023, 2003–2013, and 2013–2023.

Over the 2003–2023 study period, global biomass burning CO₂ emissions are characterized not by a significant long-term trend but by pronounced interannual variability. Specifically, the time series of global annual CO₂ emissions, derived from the MBEI, which integrates eight sub-inventories, shows no statistically significant long-term trend ($p > 0.05$; Fig. 4a). This pattern of high interannual variability, coupled with a lack of a significant long-term trend, is also observed for other major emitted species (Fig. S9). This strong interannual variability is a well-documented feature of global fire activity, primarily linked to climate anomalies such as the El Niño-Southern Oscillation (ENSO) (Chen et al., 2017; Mariani et al., 2016; Li et al., 2023). Our time-series analysis confirms this link: emission peaks (e.g., 2010, 2015,

2019) consistently coincide with major El Niño events that trigger widespread drought, while emission troughs (e.g., 2009, 2022) align with wetter La Niña conditions. The sharp contrast between the low emissions during the 2022 La Niña and the subsequent spike during the 2023 El Niño starkly illustrates the powerful influence of the ENSO cycle on global fire activity.

Alongside these climate-driven variations, the MBEI is characterized by a broad uncertainty range, stemming from differences in algorithm structures and input data. The spread between MBEI estimates (the Max-Min band in Figs. 4a, c, e) is considerable, with the difference between the highest and lowest annual totals exceeding 2600 Tg in some years (e.g., 2004, 2022). This divergence arises from methodological differences, particularly between top-down (FRP-based) and bottom-up (burned area-based) approaches in areas like fire detection and combustion parameterization. Critically, however, despite the large spread in absolute emission values, the MBEI sub-inventories show strong agreement on the relative interannual patterns, consistently identifying the same peak and trough years.

This apparent global stability masks significant and opposing regional trends, producing a highly heterogeneous spatial pattern of change (Fig. 4b). Over the full 21-year period, statistically significant trends were concentrated in Asia. BOAS exhibited a strong and significant increasing trend in emission flux at a rate of $15.71 \text{ g m}^{-2} \text{ yr}^{-1}$ ($p < 0.01$). In contrast, CEAS and SEAS showed significant decreasing trends of $-1.72 \text{ g m}^{-2} \text{ yr}^{-1}$ ($p < 0.01$) and $-2.08 \text{ g m}^{-2} \text{ yr}^{-1}$ ($p < 0.05$), respectively (Table S6). Fig. 4b suggests decreases in equatorial Africa and central-southern South America, and increases in BONA, these trends were not statistically significant when aggregated over the entire 14 GFED regions for the 2003–2023 period. This highlights an offsetting pattern, where declining emissions in some regions are partially balanced by increases elsewhere, contributing to the lack of a significant global trend.

A decadal comparison between 2003–2013 and 2013–2023 reveals substantial evolution in these spatial patterns, indicating a major shift in the global distribution of biomass burning emissions (Figs. 4d, f).

During the first decade (2003–2013), a slight but statistically non-significant global decrease ($p > 0.05$; Fig. 4c) masked a profound spatial redistribution of fire activity. The dominant feature was a significant increase in fire emissions in SHAF, which saw an upward trend of $4.41 \text{ g m}^{-2} \text{ yr}^{-1}$ ($p < 0.05$). By contrast, South America experienced significant decreases, particularly in NHSA where emissions declined at a rate of $-4.97 \text{ g m}^{-2} \text{ yr}^{-1}$ ($p < 0.05$). Simultaneously, a strong decreasing trend was observed in CEAS, with a rate of $-2.96 \text{ g m}^{-2} \text{ yr}^{-1}$ ($p < 0.05$). Boreal regions and Southeast Asia showed no statistically significant regional trends during this period (Fig. 4d and Table S7).

In the subsequent decade (2013–2023), this pattern shifted markedly. Although the global emission trajectory did not exhibit a statistically significant linear trend ($p > 0.05$), it transitioned from a slight decline to an overall increase (Fig. 4e), signaling a clear decadal change in biomass burning dynamics. This shift is more appropriately characterized as a structural transformation rather than a linear progression, driven by a marked increase in both the frequency and intensity of extreme emission years (e.g., 2015, 2019, 2023). The 2015–2016 ENSO cycle exemplifies this mechanism, as the super El Niño event in 2015 induced catastrophic PEAT in Indonesia (EQAS) and elevated global emissions to a record peak, which was subsequently followed by a pronounced decline in 2016 with the onset of a strong La Niña (Whitburn et al., 2016; Yin et al., 2020a). The 2023 fire season was even more pronounced, as an unprecedented wildfire season in boreal Canada (BONA) coincided with a developing El Niño, jointly driving global annual emissions to the highest level in our 21-year record. Detailed regional statistics, including the annual mean CO₂ emission fluxes and their corresponding Theil-Sen slope trends across the 14 study regions for the 2013–2023 period, are summarized in Table S8 (Jain et al., 2024; Luo et al., 2025).

Spatially, this decadal shift is characterized by a reversal of trends in Africa and South America (Fig. 4f). Africa, which previously showed increasing trends in the south, now exhibited a pronounced and significant decrease in NHAF, with emissions declining at $-5.14 \text{ g m}^{-2} \text{ yr}^{-1}$ ($p < 0.05$). In a direct reversal of the previous decade, SHSA showed a strong and significant increase of $8.01 \text{ g m}^{-2} \text{ yr}^{-1}$ ($p < 0.01$). Notably, despite the visually striking increases in BONA and northern Eurasia driven by the extreme fire years mentioned previously, the linear trends for these aggregated regions over the 2013–2023 period were not statistically significant, suggesting that the changes were dominated by episodic events rather than a consistent year-over-year increase.

In summary, beneath the overall stable trend of global biomass burning emissions over the past 21 years, there lies a key decadal shift, from a declining phase dominated by weakening fire activity in the tropics (2003–2013) to an increasing phase driven by intensifying fire activity in high-latitude regions and parts of the Southern Hemisphere (2013–2023).

3.4 Inter-comparison with other inventories

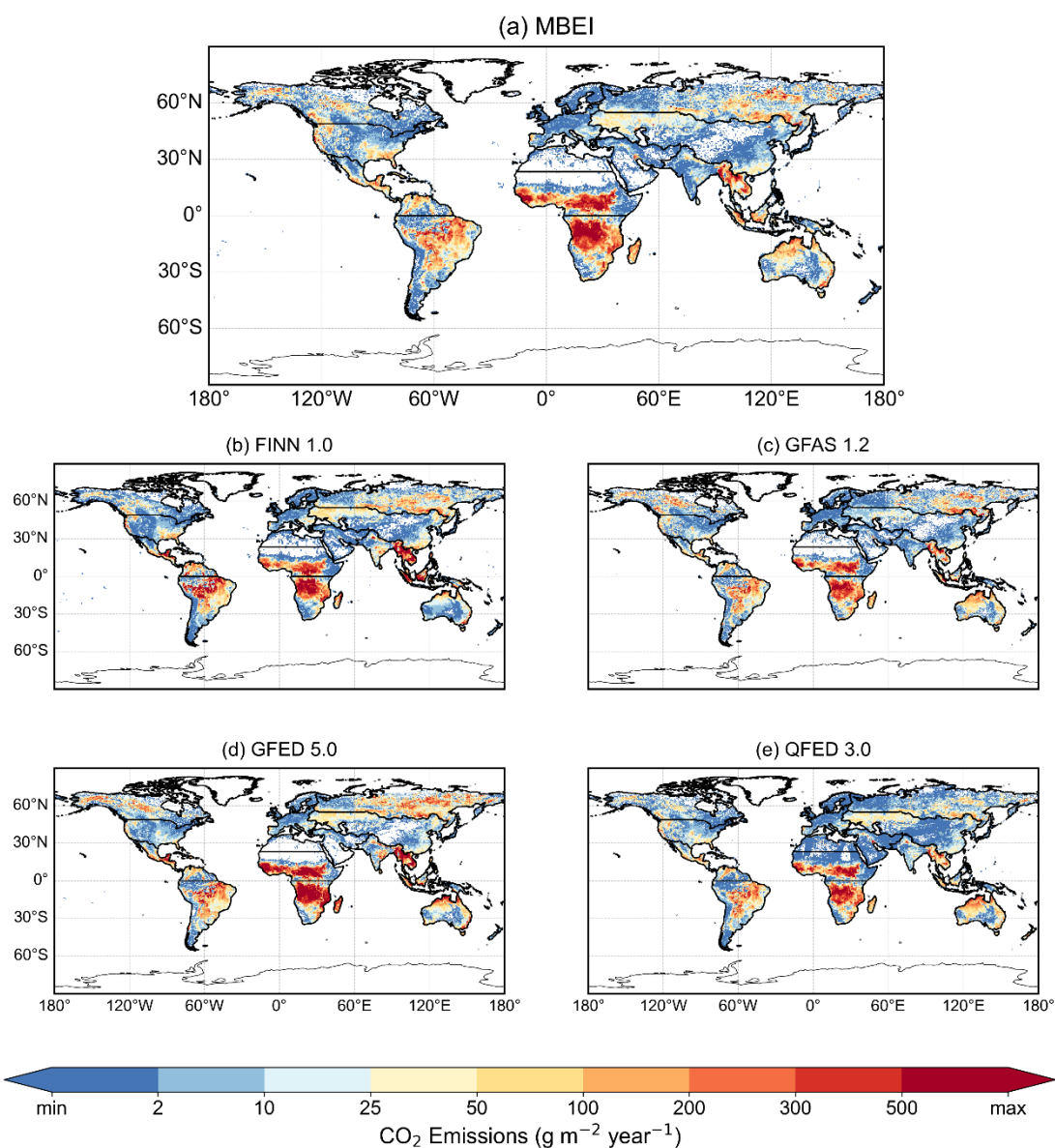


Figure 5. Comparison of multi-year mean spatial patterns of global CO₂ emissions estimated by different biomass burning inventories (2003–2022). (a) The mean of the eight inventories constructed in this study. (b) Fire INventory from NCAR version 2.5 (FINN 2.5), (c) Global Fire Assimilation System version 1.2 (GFAS 1.2), (d) Global Fire Emissions Database version 5.0 (GFED 5.0), and (e) Quick Fire Emissions Dataset version 3.1 (QFED 3.1).

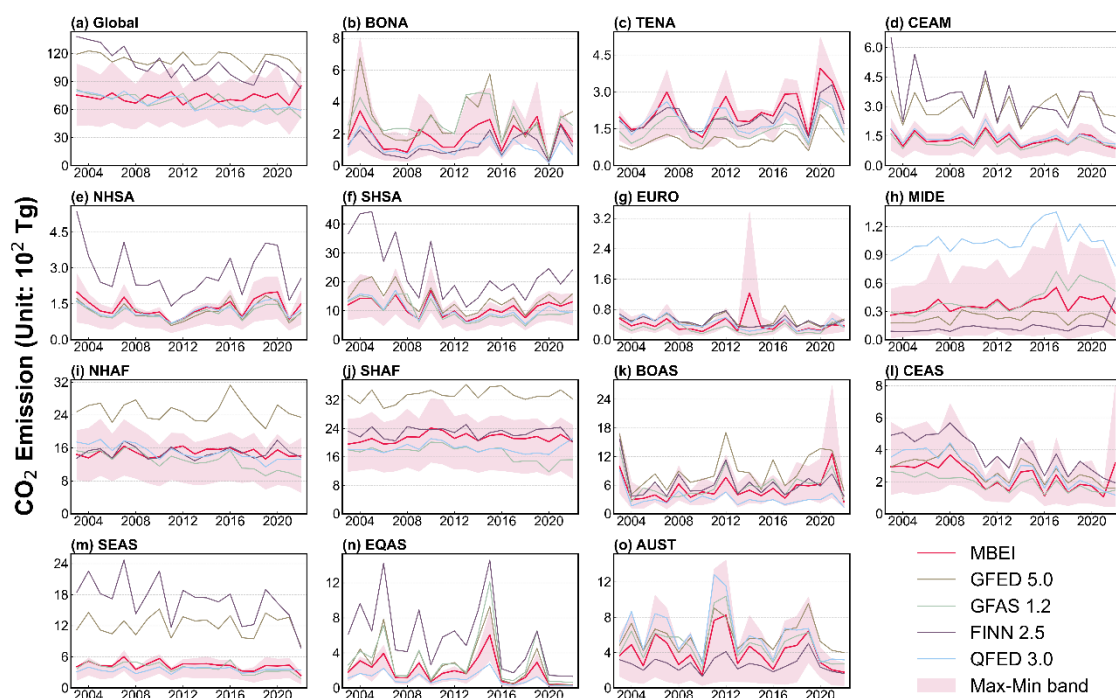


Figure 6. Time series of interannual variability in biomass burning CO₂ emissions from different inventories at global and regional scales (2003–2022). (a) Total annual global CO₂ emissions from this study's inventory and four other inventories. (b) to (o) Total annual CO₂ emissions from this study's inventory and four other inventories across 14 regions.

A comparison of biomass burning CO₂ emissions reveals broad spatial agreement across all inventories (including the MBEI from this study, FINN 2.5, GFAS 1.2, GFED 5.0, and QFED 3.1) (Fig. 5). Furthermore, the emission magnitudes from these inventories are largely consistent, with no significant discrepancies. In addition, comparative analyses are performed for three emission species, namely SO₂, PM_{2.5} and BC and the results are presented in Figs. S10–S15 in the Supplementary Material. These species represent different components and combustion phases of biomass burning. SO₂ reflects the combustion of naturally occurring sulfur-containing organic matter and inorganic sulfides in biomass, PM_{2.5} represents the overall intensity of total particulate matter emissions, and BC indicates incomplete combustion during the high-temperature flaming phase. Similar to CO₂, the spatial patterns for these species are largely consistent across inventories. While the products capture similar interannual variability, their estimates of emission magnitudes reveal substantial inter-inventory uncertainty (results show in Figs. S10–S15). All products successfully identify the primary global fire hotspots, including those in Africa (SHAF, NHAF), South America (SHSA), Southeast Asia (SEAS), and the northern boreal forests (BONA, BOAS).

However, significant discrepancies exist in both emission magnitude and spatial detail among various inventories (Fig. 6). The uncertainty range (Max-Min band) of the MBEI generally encompasses the estimates from all reference products across most regions, suggesting that it effectively captures the structural uncertainty among inventories. Moreover, the mean estimate of the MBEI typically resides near the center of the various inventories. With respect to magnitude and trend, our inventory exhibits the closest alignment with GFAS. GFED consistently provides the highest global estimates, while FINN ranks second and in some regions even exceeds GFED, whereas QFED remains generally lower. Despite these differences in magnitude, all inventories demonstrate strong consistency in interannual variability, successfully capturing major global fire years (e.g., 2010, 2015, 2019).

A regional analysis highlights significant divergences among emission inventories, particularly in the high-emission tropics where the MBEI's uncertainty band is often substantial. In the African savannas (NHAF, SHAF), the MBEI mean estimate is consistently lower than GFED 5.0, often residing in the lower half of the inter-inventory range (Figs. 6i, j). For instance, in SHAF, GFED 5.0 estimates are frequently approximately 10 Tg yr^{-1} higher than the MBEI mean, while our estimate aligns closely with GFAS 1.2 and QFED 3.0. Conversely, in regions with significant DEFO and AGRI fires like SHSA and SEAS, FINN 2.5 estimates consistently occupy the upper portion of the inter-inventory range. In these areas, the MBEI mean is again more conservative, and our Max-Min band effectively captures the cluster of lower estimates from GFED, GFAS, and QFED (Figs. 6f, m).

In contrast, inter-inventory agreement is generally higher in low- to moderate-emission regions at mid- to high latitudes, where the MBEI mean closely tracks the multi-inventory average (e.g., Temperate North American (TENA) and EURO; Figs. 6c, 6g). However, this consistency breaks down in boreal forests during years with episodic, large-scale fires. In these instances, the value of the Max-Min band becomes particularly evident. During the extreme BONA fire year of 2004, estimates spanned a wide range from FINN 2.5 (2.2 Tg) to GFED 5.0 (6.7 Tg). Critically, our own Max-Min band for that year expanded dramatically (from 1.0 to 8.0 Tg), explicitly quantifying the immense challenge and uncertainty in capturing such events. A similar expansion of our uncertainty band is observed in BOAS during its severe 2021 fire season, where our maximum estimate reached 26.8 Tg, encompassing the high values from other inventories.

Regions dominated by specific fuel types, such as the peatlands of EQAS, reveal fundamental methodological differences that are well-framed by our uncertainty analysis. While all inventories

captured the 2015 El Niño-driven fire peak, the estimated magnitude varied by more than five-fold, from QFED 3.0 (2.7 Tg) to FINN 2.5 (14.6 Tg) (Fig. 6n). The MBEI mean estimate (6.0 Tg) and its associated uncertainty band (3.2–8.6 Tg) are positioned centrally among these estimates, with its upper bound approaching the GFED 5.0 value (9.3 Tg) while excluding the extreme high and low outliers. This indicates that, under substantial uncertainty in quantifying PEAT emissions, the MBEI delineates a comprehensive Max–Min band and provides a stable central mean estimate within it.

In summary, our comparison demonstrates that while existing inventories agree on broad spatiotemporal patterns, significant quantitative disagreements persist, particularly in tropical regions and during extreme fire events. Against this backdrop, the MBEI provides a new, synthesized central estimate and a robust uncertainty range (Max–Min band). Its central estimate is consistent with the ensemble median, and its uncertainty bounds effectively encompass the spread across different inventories. This central estimate and a quantified uncertainty range not only offers a reliable measure of biomass burning emissions but also serves as a diagnostic tool, highlighting the specific regions (e.g., African savannas, Southeast Asian peatlands) and conditions (e.g., extreme boreal fires) that drive the largest inter-inventory discrepancies, thereby providing a clear basis for future inventory refinement.

4 Discussion

4.1 Advancement and uncertainty assessment

This study introduces the MBEI, a systematic emission estimation framework built upon a framework of eight sub-inventories, integrating both bottom-up and top-down approaches with various combinations of key input data. The emission range of the MBEI provides a direct measure of structural uncertainty, allowing modelers to assess the sensitivity of their simulations to inventory choice (high-end vs. low-end estimates). This addresses a long-standing challenge in climate and atmospheric chemistry modeling, where discrepancies among emission inventories are a recognized major source of the simulation uncertainty (Pan et al., 2020; Su et al., 2023). The MBEI framework systematically quantifies this uncertainty, revealing two key findings. First, the uncertainty is substantial in magnitude, with the maximum global annual CO₂ estimate across the sub-inventories being 2.2 times the minimum. Second, and perhaps more importantly, the uncertainty exhibits significant spatial heterogeneity, with the highest

relative uncertainty not coinciding with traditional emission hotspots, but instead found in regions with lower emissions, such as AUST and MIDE.

This divergence is strongly linked to how regional land cover and fire regime characteristics amplify the sensitivity of different estimation methodologies. For instance, in AUST, the fire regime is dominated by event-driven, extremely high-intensity megafires. These events pose significant challenges for both FRP-based algorithms, which can be prone to saturation, and burned area-based methods, which struggle to accurately map such intense and rapidly spreading fires. Conversely, in the MIDE, the high uncertainty arises from weak, small-scale, and scattered AGRI or SAVA. These fires are often near the detection limits of satellite sensors, causing emission estimates to be highly sensitive to the chosen active fire detection confidence thresholds. In stark contrast, African savannas, despite their high emission fluxes, show lower relative uncertainty. Their widespread and seasonally predictable fires are robustly captured by both top-down and bottom-up approaches, leading to greater convergence among the different methods. This finding implies that future efforts to refine emission inventories should extend beyond traditional hotspots to better understand and parameterize the distinct combustion processes in these atypical fire regimes.

The MBEI's 21-year analysis also uncovers a critical shift in the long-term dynamics of global emissions. Despite a stable trend overall, we identify a clear decadal transition: from a slight decline dominated by weakening tropical fires (2003–2013) to a rising phase driven by intensifying boreal fires and more frequent extreme events (2013–2023). This dynamic, characterized by a decline in tropical fire activity and an increase in boreal fire activity, synthesizes seemingly disparate observations, such as the global decrease in burned area (Andela et al., 2017) and the lengthening of fire seasons in high-latitude regions (Jones et al., 2022), into a coherent narrative at the emission level. Particularly in the second decade, climate-driven extreme events, such as the 2015 Indonesian peat fires, the 2019–2020 Australian megafires, and the 2023 Canadian wildfires, significantly reshaped the global emission record. This underscores the growing influence of climate change on global biomass burning emissions, a shift with profound implications for the global carbon cycle and its associated climate feedbacks.

4.2 Limitations and Future Perspectives of the MBEI Framework

The MBEI framework aims to quantify the structural uncertainty in global biomass burning emissions by ensembling multiple algorithmic approaches. However, the accuracy of any emission inventory is inherently constrained by the spatiotemporal resolution and physical sensitivity of its input data. The

uncertainty ranges revealed in this study, which span various regions and biomes, largely reflect the physical limitations of current Earth observation systems in capturing extreme fire behaviors and complex surface processes, alongside the methodological differences discussed.

A key decision in this study was to use MODIS active fire products (MCD14DL) exclusively for the 2003–2023 period. Although the Visible Infrared Imaging Radiometer Suite (VIIRS), available since 2012, offers superior spatial resolution (375 m) compared to MODIS (1 km), applying it would have limited the consistent time series to the post-2012 era. Merging MODIS (2003–2011) and VIIRS (2012–2023) records introduces a risk of inconsistency; the higher detection sensitivity of VIIRS could result in an artificial increase in fire counts, which might be misinterpreted as a real upward trend in global fire activity. To maintain the homogeneity of the 21-year dataset for trend analysis, we prioritized sensor consistency. We acknowledge that this choice likely leads to an underestimation of emissions from small-scale agricultural fires, particularly in regions like the Middle East or India, where fires are often smaller than the MODIS detection threshold (Hantson et al., 2013; Justice et al., 2002; Vadrevu and Lasko, 2018). In addition to sensor specifications, most current inventories relying on optical remote sensing face inherent physical limits driven by environmental heterogeneity. Complex surface conditions can constrain the effectiveness of estimation methods. For instance, in the peatlands of Equatorial Asia (e.g., Indonesia), fires often occur as subsurface low-temperature smoldering. The thermal radiation from these fires is frequently too weak to trigger standard satellite detection algorithms (Rein and Huang, 2021; Sofan et al., 2019). Similarly, in dense tropical rainforests, the canopy layer can occlude or absorb thermal radiation emitted by understory fires (East et al., 2023). These scenarios contribute to omission errors in top-down, FRP-based approaches (Morton et al., 2013; Tyukavina et al., 2022). Conversely, while bottom-up methods based on burned area can capture the spatial traces of these fires, they face challenges in accurately determining the depth of burn in organic soils (Ballhorn et al., 2009; Wiggins et al., 2018). Therefore, despite the integration of multiple algorithms in MBEI, these physical constraints suggest a potential underestimation in our emission estimates for these specific biomes.

Looking forward, the flexible architecture of MBEI is designed to incorporate emerging datasets to address these limitations. As the observational record of VIIRS extends, future versions of MBEI will integrate these data to improve the detection of small-scale fires once a sufficiently long and consistent record is established. Furthermore, data from new-generation geostationary satellites (e.g., FY-4, Himawari-8/9, GOES-R) offer a significant improvement in temporal resolution. Minute-level

observations from these platforms will enable the direct integration of the Fire Radiative Power diurnal cycle, reducing the reliance on Gaussian extrapolation from sparse polar-orbiter snapshots and enhancing the physical realism of Fire Radiative Energy estimation.

Advancements in next-generation satellites will also enhance the MBEI's capacity for fuel load estimation. In this study, due to the lack of high-resolution annual AGB observations, we adjusted static AGB maps using interannual variations in NPP. However, AGB is a cumulative stock variable, whereas NPP is an annual flux variable. Their relationship is complex and influenced by factors such as lag effects, tree mortality, and decomposition, meaning a high NPP year does not always result in an immediate biomass increase (Keeling and Phillips, 2007; Teets et al., 2022). Future versions of MBEI aim to improve this by integrating dynamic AGB datasets from active remote sensing missions. Specifically, spaceborne LiDAR (e.g., NASA GEDI) and P-band SAR (e.g., ESA BIOMASS mission) are expected to provide global measurements of forest vertical structure. This will allow MBEI to incorporate dynamic fuel loads, thereby reducing a major source of uncertainty in the bottom-up approach based on burned area (Cao et al., 2016; Liu et al., 2019; Rodríguez-Fernández et al., 2018).

Finally, current emission estimates rely on static EFs, which may not fully capture the variability of combustion efficiency within biomes or during a fire's lifecycle (van Leeuwen et al., 2013; Yin, 2022). Future improvements are expected to come from developing comprehensive EF databases through advanced molecular-level aerosol speciation (Jen et al., 2019; Koss et al., 2018). Complementing this, dynamic high-resolution EF datasets could be generated using synchronous satellite trace gas retrievals. For example, the ratio of carbon monoxide to nitrogen dioxide ($\Delta\text{NO}_2 / \Delta\text{CO}$) columns derived from the TROPOMI sensor can serve as a near-real-time proxy for combustion efficiency (flaming vs. smoldering) (van der Velde et al., 2021). By assimilating such dynamic proxies, MBEI aims to evolve toward a more dynamic monitoring system.

In conclusion, while the current version of MBEI quantifies uncertainty by integrating established methods, its modular design serves as a platform for incorporating new data inputs as they become available. This ensures a feasible pathway for iterative refinement, supporting more comprehensive assessments of global biomass burning emissions.

5 Conclusion

This study systematically assessed global biomass burning emissions and their uncertainties from 2003–2023 using the MBEI, an ensemble framework of eight sub-inventories that integrates both bottom-up and top-down approaches. A key finding is the spatial separation between the emission hotspots and the uncertainty hotspots. While high-emission regions in Africa and South America account for 64.4% of global CO₂ emissions, the structural uncertainty there is relatively constrained (max/min ratio < 2.0). In contrast, the greatest uncertainty (max/min ratio > 6.0) is found in lower-emission regions characterized by extreme, intermittent fires (e.g., AUST) or scattered agricultural burning (e.g., the MIDE).

Temporally, our analysis reveals a significant shift in the drivers of global biomass burning emissions over the past two decades. Although the overall long-term trend is not statistically significant, we identify a clear transition: the period dominated by declining tropical fire activity (2003–2013) was followed by a period increasingly influenced by intensifying high-latitude boreal fires and frequent climate-driven extreme events (2013–2023).

The spatial heterogeneity and temporal shift highlight the growing complexity of the global biomass burning emission regimes. The primary contribution of the MBEI framework is therefore its ability to explicitly quantify this structural uncertainty. It provides a central estimate consistent with the multi-inventory average, along with an uncertainty range that encompasses the estimates of major existing products. MBEI offers the crucial boundary conditions needed for Earth system models to estimate related environmental or exposure risk.

To effectively assess the complex dynamics of global biomass burning emission, the results of this study indicate that the focus should evolve from pursuing a single best estimate to embracing a probabilistic, uncertainty-aware approach. It is suggested that such data-constrained uncertainty information should be directly integrated into atmospheric chemistry and Earth system models. This is essential not only for improving model fidelity but also for conducting more robust risk assessments that consider plausible high-end emission scenarios. Ultimately, the MBEI's explicit quantification of uncertainty provides a more solid scientific foundation for developing resilient environmental and climate policies.

Data availability. The developed MBEI emission inventory described in this paper is available from Zenodo: 10.5281/zenodo.18104830 (Liu and Yin, 2025). For further support or guidance regarding data use, please contact yinshuai@aircas.ac.cn.

Supplement.

Author contributions. SY and ZS were responsible for the conceptualization of the study, project administration, supervision, and funding acquisition. XL designed the methodology, developed the software, performed the formal analysis and investigation, curated the data, prepared the visualizations and wrote the original draft of the manuscript. CS contributed to the methodology development and software implementation. TN, PW, QC and LS assisted with the formal analysis and data curation. HS, DJ, MG, KY, ZT, LW, and XL contributed to the investigation, validation, and provision of resources. All authors participated in the review and editing of the manuscript and have approved the final version for publication.

Competing interests. The contact author has declared that none of the authors has any competing interests.

Disclaimer. Publisher's note: Copernicus Publications remains neutral with regard to jurisdictional claims in published maps and institutional affiliations. While Copernicus Publications makes every effort to ensure appropriate place names are included, the final responsibility lies with the authors.

Acknowledgements. The authors would like to thank J. W. Kaiser for providing access to the most recent data. We also acknowledge the support of the State Key Laboratory of Remote Sensing and Digital Earth, Aerospace Information Research Institute, Chinese Academy of Sciences. The authors extend their gratitude to the anonymous reviewers for their constructive comments, which greatly helped improve the quality of this paper.

Financial support. This research is supported by the National Natural Science Foundation of China (grant no. 42475142).

Reference

Andela, N., Kaiser, J. W., van der Werf, G. R., and Wooster, M. J.: New fire diurnal cycle characterizations to improve fire radiative energy assessments made from MODIS observations, *Atmospheric Chemistry and Physics*, 15, 8831–8846, <https://doi.org/10.5194/acp-15-8831-2015>, 2015.

Andela, N., Morton, D. C., Giglio, L., Chen, Y., van der Werf, G. R., Kasibhatla, P. S., DeFries, R. S., Collatz, G. J., Hantson, S., Kloster, S., Bachelet, D., Forrest, M., Lasslop, G., Li, F., Mangeon, S., Melton, J. R., Yue, C., and Randerson, J. T.: A human-driven decline in global burned area, *Science*, 356, 1356–1362, <https://doi.org/10.1126/science.aal4108>, 2017.

Andreae, M. O. and Merlet, P.: Emission of trace gases and aerosols from biomass burning, *Global Biogeochemical Cycles*, 15, 955–966, <https://doi.org/10.1029/2000GB001382>, 2001.

Andreae, M. O.: Emission of trace gases and aerosols from biomass burning – an updated assessment, *Atmospheric Chemistry and Physics*, 19, 8523–8546, <https://doi.org/10.5194/acp-19-8523-2019>, 2019.

Ballhorn, U., Siegert, F., Mason, M., and Limin, S.: Derivation of burn scar depths and estimation of carbon emissions with LIDAR in Indonesian peatlands, *Proceedings of the National Academy of Sciences*, 106, 21213–21218, <https://doi.org/10.1073/pnas.0906457106>, 2009.

Binte Shahid, S., Lacey, F. G., Wiedinmyer, C., Yokelson, R. J., and Barsanti, K. C.: NEIVAv1.0: Next-generation emissions inventory expansion of Akagi et al. (2011) version 1.0, *Geoscientific Model Development*, 17, 7679–7711, <https://doi.org/10.5194/gmd-17-7679-2024>, 2024.

Bowman, D. M. J. S., Balch, J. K., Artaxo, P., Bond, W. J., Carlson, J. M., Cochrane, M. A., D’Antonio, C. M., DeFries, R. S., Doyle, J. C., Harrison, S. P., Johnston, F. H., Keeley, J. E., Krawchuk, M. A., Kull, C. A., Marston, J. B., Moritz, M. A., Prentice, I. C., Roos, C. I., Scott, A. C., Swetnam, T. W., van der Werf, G. R., and Pyne, S. J.: Fire in the earth system, *Science*, 324, 481–484, <https://doi.org/10.1126/science.1163886>, 2009.

Bowman, D. M. J. S., Kolden, C. A., Abatzoglou, J. T., Johnston, F. H., van der Werf, G. R., and Flannigan, M.: Vegetation fires in the Anthropocene, *Nature Reviews Earth & Environment*, 1, 500–515, <https://doi.org/10.1038/s43017-020-0085-3>, 2020.

Bray, C. D., Battye, W. H., Aneja, V. P., and Schlesinger, W. H.: Global emissions of NH₃, NO_x, and N₂O from biomass burning and the impact of climate change, *Journal of the Air & Waste Management Association*, 71, 102–114, <https://doi.org/10.1080/10962247.2020.1842822>, 2021.

Cao, L., Coops, N. C., Innes, J. L., Sheppard, S. R. J., Fu, L., Ruan, H., and She, G.: Estimation of forest biomass dynamics in subtropical forests using multi-temporal airborne LiDAR data, *Remote Sensing of Environment*, 178, 158–171, <https://doi.org/10.1016/j.rse.2016.03.012>, 2016.

Chen, Y., Morton, D. C., Andela, N., van der Werf, G. R., Giglio, L., and Randerson, J. T.: A pan-tropical cascade of fire driven by el niño/southern oscillation, *Nature Climate Change*, 7, 906–911, <https://doi.org/10.1038/s41558-017-0014-8>, 2017.

Cunningham, C. X., Williamson, G. J., and Bowman, D. M. J. S.: Increasing frequency and intensity of the most extreme wildfires on earth, *Nature Ecology & Evolution*, 8, 1420–1425, <https://doi.org/10.1038/s41559-024-02452-2>, 2024.

Filonchyk, M., Peterson, M. P., Zhang, L., Hurynovich, V., and He, Y.: Greenhouse gases emissions and global climate change: Examining the influence of CO₂, CH₄, and N₂O, *Science of The Total Environment*, 935, 173359, <https://doi.org/10.1016/j.scitotenv.2024.173359>, 2024.

Friedl, M. and Sulla-Menashe, D.: MODIS/terra+aqua land cover type yearly L3 global 500m SIN grid V061, NASA LP DAAC [data set], <https://doi.org/10.5067/MODIS/MCD12Q1.061>, 2022.

East, A., Hansen, A., Armenteras, D., Jantz, P., and Roberts, D. W.: Measuring understory fire effects from space: Canopy change in response to tropical understory fire and what this means for applications of GEDI to tropical forest fire, *Remote Sensing*, 15, 696, <https://doi.org/10.3390/rs15030696>, 2023.

Friedlingstein, P., O'Sullivan, M., Jones, M. W., Andrew, R. M., Hauck, J., Landschützer, P., Le Quéré, C., Li, H., Luijckx, I. T., Olsen, A., Peters, G. P., Peters, W., Pongratz, J., Schwingshackl, C., Sitch, S., Canadell, J. G., Ciais, P., Jackson, R. B., Alin, S. R., Arneeth, A., Arora, V., Bates, N. R., Becker, M., Bellouin, N., Berghoff, C. F., Bittig, H. C., Bopp, L., Cadule, P., Campbell, K., Chamberlain, M. A., Chandra, N., Chevallier, F., Chini, L. P., Colligan, T., Decayeux, J., Djeutchouang, L. M., Dou, X., Duran Rojas, C., Enyo, K., Evans, W., Fay, A. R., Feely, R. A., Ford, D. J., Foster, A., Gasser, T., Gehlen, M., Gkritzalis, T., Grassi, G., Gregor, L., Gruber, N., Gürses, Ö., Harris, I., Hefner, M., Heinke, J., Hurtt, G. C., Iida, Y., Ilyina, T., Jacobson, A. R., Jain, A. K., Jarníková, T., Jersild, A., Jiang, F., Jin, Z., Kato, E., Keeling, R. F., Klein Goldewijk, K., Knauer, J., Korsbakken, J. I., Lan, X., Lauvset, S. K., Lefèvre, N., Liu, Z., Liu, J., Ma, L., Maksyutov, S., Marland, G., Mayot, N., McGuire, P. C., Metzl, N., Monacci, N. M., Morgan, E. J., Nakaoka, S.-I., Neill, C., Niwa, Y., Nützel, T., Olivier, L., Ono, T., Palmer, P. I., Pierrot, D., Qin, Z., Resplandy, L., Roobaert, A., Rosan, T. M., Rödenbeck, C., Schwinger, J., Smallman, T. L., Smith, S. M., Sospedra-Alfonso, R., Steinhoff, T., Sun, Q., Sutton, A. J., Séférian, R., Takao, S., Tatebe, H., Tian, H., Tilbrook, B., Torres, O., Tourigny, E., Tsujino, H., Tubiello, F., van der Werf, G., Wanninkhof, R., Wang, X., Yang, D., Yang, X., Yu, Z., Yuan, W., Yue, X., Zaehle, S., Zeng, N., and Zeng,

J.: Global carbon budget 2024, *Earth System Science Data*, 17, 965–1039, <https://doi.org/10.5194/essd-17-965-2025>, 2025.

Giglio, L., Schroeder, W., and Hall, J. V.: MODIS collection 6 active fire product user's guide revision C, NASA, available at: https://modis-fire.umd.edu/files/MODIS_C6_C6.1_Active_Fire_User_Guide_C.pdf (last access: 15 August 2025), 2020.

Giglio, L., van der Werf, G. R., Randerson, J. T., Collatz, G. J., and Kasibhatla, P.: Global estimation of burned area using MODIS active fire observations, *Atmospheric Chemistry and Physics*, 6, 957–974, <https://doi.org/10.5194/acp-6-957-2006>, 2006.

Hantson, S., Padilla, M., Corti, D., and Chuvieco, E.: Strengths and weaknesses of MODIS hotspots to characterize global fire occurrence, *Remote Sensing of Environment*, 131, 152–159, <https://doi.org/10.1016/j.rse.2012.12.004>, 2013.

Hoelzemann, J. J., Schultz, M. G., Brasseur, G. P., Granier, C., and Simon, M.: Global wildland fire emission model (GWEM): Evaluating the use of global area burnt satellite data, *Journal of Geophysical Research: Atmospheres*, 109, <https://doi.org/10.1029/2003JD003666>, 2004.

Ichoku, C. and Ellison, L.: Global top-down smoke-aerosol emissions estimation using satellite fire radiative power measurements, *Atmospheric Chemistry and Physics*, 14, 6643–6667, <https://doi.org/10.5194/acp-14-6643-2014>, 2014.

Ichoku, C. and Kaufman, Y. J.: A method to derive smoke emission rates from MODIS fire radiative energy measurements, *IEEE Transactions on Geoscience and Remote Sensing*, 43, 2636–2649, <https://doi.org/10.1109/TGRS.2005.857328>, 2005.

Ito, A. and Penner, J. E.: Global estimates of biomass burning emissions based on satellite imagery for the year 2000, *Journal of Geophysical Research: Atmospheres*, 109, <https://doi.org/10.1029/2003JD004423>, 2004.

Jain, P., Barber, Q. E., Taylor, S. W., Whitman, E., Castellanos Acuna, D., Boulanger, Y., Chavardès, R. D., Chen, J., Englefield, P., Flannigan, M., Girardin, M. P., Hanes, C. C., Little, J., Morrison, K., Skakun, R. S., Thompson, D. K., Wang, X., and Parisien, M.-A.: Drivers and impacts of the record-breaking 2023 wildfire season in Canada, *Nature Communications*, 15, 6764, <https://doi.org/10.1038/s41467-024-51154-7>, 2024.

Jen, C. N., Hatch, L. E., Selimovic, V., Yokelson, R. J., Weber, R., Fernandez, A. E., Kreisberg, N. M., Barsanti, K. C., and Goldstein, A. H.: Speciated and total emission factors of particulate organics from burning western US wildland fuels and their dependence on combustion efficiency, *Atmospheric Chemistry and Physics*, 19, 1013–1026, <https://doi.org/10.5194/acp-19-1013-2019>, 2019.

Jones, M. W., Abatzoglou, J. T., Veraverbeke, S., Andela, N., Lasslop, G., Forkel, M., Smith, A. J. P., Burton, C., Betts, R. A., van der Werf, G. R., Sitch, S., Canadell, J. G., Santín, C., Kolden, C., Doerr, S. H., and Le Quéré, C.: Global and regional trends and drivers of fire under climate change, *Reviews of Geophysics*, 60, e2020RG000726, <https://doi.org/10.1029/2020RG000726>, 2022.

Justice, C. O., Giglio, L., Korontzi, S., Owens, J., Morisette, J. T., Roy, D., Descloitres, J., Alleaume, S., Petitcolin, F., and Kaufman, Y.: The MODIS fire products, *Remote Sensing of Environment*, 83, 244–262, [https://doi.org/10.1016/S0034-4257\(02\)00076-7](https://doi.org/10.1016/S0034-4257(02)00076-7), 2002.

Kaiser, J. W., Heil, A., Andreae, M. O., Benedetti, A., Chubarova, N., Jones, L., Morcrette, J.-J., Razinger, M., Schultz, M. G., Suttie, M., and van der Werf, G. R.: Biomass burning emissions estimated with a global fire assimilation system based on observed fire radiative power, *Biogeosciences*, 9, 527–554, <https://doi.org/10.5194/bg-9-527-2012>, 2012.

Kaiser, J. W., Holmedal, D. G., Ytre-Eide, M. A., and de Jong, M.: GFAS4HTAP vegetation fire emissions 2003-2023, Zenodo [data set], <https://doi.org/10.5281/zenodo.15721463>, 2023.

Karanasiou, A., Alastuey, A., Amato, F., Renzi, M., Stafoggia, M., Tobias, A., Reche, C., Forastiere, F., Gumy, S., Mudu, P., and Querol, X.: Short-term health effects from outdoor exposure to biomass burning emissions: A review, *Science of The Total Environment*, 781, 146739, <https://doi.org/10.1016/j.scitotenv.2021.146739>, 2021.

Keeling, H. C. and Phillips, O. L.: The global relationship between forest productivity and biomass, *Global Ecology and Biogeography*, 16, 618–631, <https://doi.org/10.1111/j.1466-8238.2007.00314.x>, 2007.

Koss, A. R., Sekimoto, K., Gilman, J. B., Selimovic, V., Coggon, M. M., Zarzana, K. J., Yuan, B., Lerner, B. M., Brown, S. S., Jimenez, J. L., Krechmer, J., Roberts, J. M., Warneke, C., Yokelson, R. J., and de Gouw, J.: Non-methane organic gas emissions from biomass burning: Identification, quantification, and emission factors from PTR-ToF during the FIREX 2016 laboratory experiment, *Atmospheric Chemistry and Physics*, 18, 3299–3319, <https://doi.org/10.5194/acp-18-3299-2018>, 2018.

Koster, R. D., Darmenov, A. S., and da Silva, A. M.: The quick fire emissions dataset (QFED): Documentation of versions 2.1, 2.2 and 2.4: technical report series on global modeling and data assimilation - volume 38, NASA, available at: <https://ntrs.nasa.gov/citations/20180005253> (last access: 15 August 2025), 2015.

Letu, H., Ma, R., Nakajima, T. Y., Shi, C., Hashimoto, M., Nagao, T. M., Baran, A. J., Nakajima, T., Xu, J., Wang, T., Tana, G., Bilige, S., Shang, H., Chen, L., Ji, D., Lei, Y., Wei, L., Zhang, P., Li, J., Li, L., Zheng, Y., Khatri, P., and Shi, J.: Surface solar radiation compositions observed from himawari-8/9 and fengyun-4 series, *Bulletin of the American Meteorological Society*, 104, E1839–E1856, <https://doi.org/10.1175/BAMS-D-22-0154.1>, 2023.

Li, K., Zheng, F., Cheng, L., Zhang, T., and Zhu, J.: Record-breaking global temperature and crises with strong El Niño in 2023–2024, *The Innovation Geoscience*, 1, 100030, doi:10.59717/j.xinn-geo.2023.100030, 2023.

Liu, T., Mickley, L. J., Marlier, M. E., DeFries, R. S., Khan, M. F., Latif, M. T., and Karambelas, A.: Diagnosing spatial biases and uncertainties in global fire emissions inventories: Indonesia as regional case study, *Remote Sensing of Environment*, 237, 111557, <https://doi.org/10.1016/j.rse.2019.111557>, 2020.

Liu, X. and Yin, S.: Multi-ensemble Biomass-burning Emissions Inventory (MBEI)_v1.0, Zenodo [data set], <https://doi.org/10.5281/zenodo.18104830>, 2025.

Liu, Y., Chen, J., Shi, Y., Zheng, W., Shan, T., and Wang, G.: Global emissions inventory from open biomass burning (GEIOBB): Utilizing fengyun-3D global fire spot monitoring data, *Earth System Science Data*, 16, 3495–3515, <https://doi.org/10.5194/essd-16-3495-2024>, 2024.

Liu, Y., Gong, W., Xing, Y., Hu, X., and Gong, J.: Estimation of the forest stand mean height and aboveground biomass in northeast China using SAR sentinel-1B, multispectral sentinel-2A, and DEM imagery, *ISPRS Journal of Photogrammetry and Remote Sensing*, 151, 277–289, <https://doi.org/10.1016/j.isprsjprs.2019.03.016>, 2019.

Longo, K. M., Freitas, S. R., Andreae, M. O., Setzer, A., Prins, E., and Artaxo, P.: The coupled aerosol and tracer transport model to the brazilian developments on the regional atmospheric modeling system (CATT-BRAMS) – part 2: Model sensitivity to the biomass burning inventories, *Atmospheric Chemistry and Physics*, 10, 5785–5795, <https://doi.org/10.5194/acp-10-5785-2010>, 2010.

Luo, B., Xiao, C., Luo, D., Fu, Q., Chen, D., Zhang, Q., Ge, Y., and Diao, Y.: Atmospheric and oceanic drivers behind the 2023 canadian wildfires, *Communications Earth & Environment*, 6, 446, <https://doi.org/10.1038/s43247-025-02387-x>, 2025.

Mann, H. B.: Nonparametric tests against trend, *Econometrica*, 13, 245–259, <https://doi.org/10.2307/1907187>, 1945.

Mariani, M., Fletcher, M.-S., Holz, A., and Nyman, P.: ENSO controls interannual fire activity in southeast australia, *Geophysical Research Letters*, 43, 10891–10900, <https://doi.org/10.1002/2016GL070572>, 2016.

Matthias, V., Arndt, Jan A., Aulinger, Armin, Bieser, Johannes, Denier van der Gon, Hugo, Kranenburg, Richard, Kuenen, Jeroen, Neumann, Daniel, Pouliot, George, and Quante, M.: Modeling emissions for three-dimensional atmospheric chemistry transport models, *Journal of the Air & Waste Management Association*, 68, 763–800, <https://doi.org/10.1080/10962247.2018.1424057>, 2018.

Mieville, A., Granier, C., Liousse, C., Guillaume, B., Mouillot, F., Lamarque, J.-F., Grégoire, J.-M., and Pétron, G.: Emissions of gases and particles from biomass burning during the 20th century using satellite data and an historical reconstruction, *Atmospheric Environment*, 44, 1469–1477, <https://doi.org/10.1016/j.atmosenv.2010.01.011>, 2010.

Morton, D. C., Le Page, Y., DeFries, R., Collatz, G. J., and Hurtt, G. C.: Understorey fire frequency and the fate of burned forests in southern Amazonia, *Philosophical Transactions of the Royal Society B: Biological Sciences*, 368, 20120163, <https://doi.org/10.1098/rstb.2012.0163>, 2013.

N'Datchoh, T. E., Liousse, C., Roblou, L., and N'Dri, A. B.: Biomass burning over africa: How to explain the differences observed between the different emission inventories?, *Atmosphere*, 16, 440, <https://doi.org/10.3390/atmos16040440>, 2025.

NASA VIIRS Land Science Team: VIIRS (NOAA-21/JPSS-2) I band 375 m active fire product NRT (vector data), NASA FIRMS [data set], <https://doi.org/10.5067/FIRMS/MODIS/MCD14DL.NRT.0061>, 2021.

Pan, X., Ichoku, C., Chin, M., Bian, H., Darmenov, A., Colarco, P., Ellison, L., Kucsera, T., da Silva, A., Wang, J., Oda, T., and Cui, G.: Six global biomass burning emission datasets: Intercomparison and application in one global aerosol model, *Atmospheric Chemistry and Physics*, 20, 969–994, <https://doi.org/10.5194/acp-20-969-2020>, 2020.

Pellegrini, A. F. A., Ahlström, A., Hobbie, S. E., Reich, P. B., Nieradzik, L. P., Staver, A. C., Scharenbroch, B. C., Jumpponen, A., Anderegg, W. R. L., Randerson, J. T., and Jackson, R. B.: Fire frequency drives decadal changes in soil carbon and nitrogen and ecosystem productivity, *Nature*, 553, 194–198, <https://doi.org/10.1038/nature24668>, 2018.

Pereira, G., Siqueira, R., Rosário, N. E., Longo, K. L., Freitas, S. R., Cardozo, F. S., Kaiser, J. W., and Wooster, M. J.: Assessment of fire emission inventories during the south American biomass burning analysis (SAMBBA) experiment, *Atmospheric Chemistry and Physics*, 16, 6961–6975, <https://doi.org/10.5194/acp-16-6961-2016>, 2016.

Raich, J. W., Russell, A. E., Kitayama, K., Parton, W. J., and Vitousek, P. M.: Temperature influences carbon accumulation in moist tropical forests, *Ecology*, 87, 76–87, <https://doi.org/10.1890/05-0023>, 2006.

Ramanathan, V. and Carmichael, G.: Global and regional climate changes due to black carbon, *Nature Geoscience*, 1, 221–227, <https://doi.org/10.1038/ngeo156>, 2008.

Reid, J. S., Koppmann, R., Eck, T. F., and Eleuterio, D. P.: A review of biomass burning emissions part II: Intensive physical properties of biomass burning particles, *Atmospheric Chemistry and Physics*, 5, 799–825, <https://doi.org/10.5194/acp-5-799-2005>, 2005.

Rein, G. and Huang, X.: Smouldering wildfires in peatlands, forests and the Arctic: Challenges and perspectives, *Current Opinion in Environmental Science & Health*, 24, 100296, <https://doi.org/10.1016/j.coesh.2021.100296>, 2021.

Rodríguez-Fernández, N. J., Mialon, A., Mermoz, S., Bouvet, A., Richaume, P., Al Bitar, A., Al-Yaari, A., Brandt, M., Kaminski, T., Le Toan, T., Kerr, Y. H., and Wigneron, J.-P.: An evaluation of SMOS L-band vegetation optical depth (L-VOD) data sets: High sensitivity of L-VOD to above-ground biomass in africa, *Biogeosciences*, 15, 4627–4645, <https://doi.org/10.5194/bg-15-4627-2018>, 2018.

Running, S. and Zhao, M.: MODIS/aqua net primary production gap-filled yearly L4 global 500m SIN grid V061, NASA Land Processes Distributed Active Archive Center (LP DAAC) [data set], <https://doi.org/10.5067/MODIS/MYD17A3HGF.061>, 2021.

Santoro, M. and Cartus, O.: ESA biomass climate change initiative (biomass_cci): Global datasets of forest above-ground biomass for the years 2010, 2015, 2016, 2017, 2018, 2019, 2020 and 2021, v5.01 (5.01), Centre for Environmental Data Analysis (CEDA) [data set], <https://doi.org/10.5285/bf535053562141c6bb7ad831f5998d77>, 2024.

Santoro, M.: GlobBiomass - global datasets of forest biomass, PANGAEA [data set], <https://doi.org/10.1594/PANGAEA.894711>, 2018.

Seiler, W. and Crutzen, P. J.: Estimates of gross and net fluxes of carbon between the biosphere and the atmosphere from biomass burning, *Climatic Change*, 2, 207–247, <https://doi.org/10.1007/BF00137988>, 1980.

Sen, P. K.: Estimates of the regression coefficient based on kendall's tau, *Journal of the American Statistical Association*, 63, 1379–1389, <https://doi.org/10.1080/01621459.1968.10480934>, 1968.

Senande-Rivera, M., Insua-Costa, D., and Miguez-Macho, G.: Spatial and temporal expansion of global wildland fire activity in response to climate change, *Nature Communications*, 13, 1208, <https://doi.org/10.1038/s41467-022-28835-2>, 2022.

Shi, C., Letu, H., et al.: Near-global monitoring of surface solar radiation through the construction of a geostationary satellite network observation system, *The Innovation*, 6, 100876, <https://doi.org/10.1016/j.xinn.2025.100876>, 2025.

Shi, Y. and Matsunaga, T.: Temporal comparison of global inventories of CO₂ emissions from biomass burning during 2002–2011 derived from remotely sensed data, *Environmental Science and Pollution Research*, 24, 16905–16916, <https://doi.org/10.1007/s11356-017-9141-z>, 2017.

Shi, Y., Matsunaga, T., Saito, M., Yamaguchi, Y., and Chen, X.: Comparison of global inventories of CO₂ emissions from biomass burning during 2002–2011 derived from multiple satellite products, *Environmental Pollution*, 206, 479–487, <https://doi.org/10.1016/j.envpol.2015.08.009>, 2015.

Silva, S. S. da, Fearnside, P. M., Graça, P. M. L. de A., Brown, I. F., Alencar, A., and Melo, A. W. F. de: Dynamics of forest fires in the southwestern amazon, *Forest Ecology and Management*, 424, 312–322, <https://doi.org/10.1016/j.foreco.2018.04.041>, 2018.

Sofan, P., Bruce, D., Jones, E., and Marsden, J.: Detection and validation of tropical peatland flaming and smouldering using Landsat-8 SWIR and TIRS bands, *Remote Sensing*, 11, 465, <https://doi.org/10.3390/rs11040465>, 2019.

Stroppiana, D., Brivio, P. A., Grégoire, J.-M., Lioussé, C., Guillaume, B., Granier, C., Mieville, A., Chin, M., and Pétron, G.: Comparison of global inventories of CO emissions from biomass burning derived from remotely sensed data, *Atmospheric Chemistry and Physics*, 10, 12173–12189, <https://doi.org/10.5194/acp-10-12173-2010>, 2010.

Su, M., Shi, Y., Yang, Y., and Guo, W.: Impacts of different biomass burning emission inventories: Simulations of atmospheric CO₂ concentrations based on GEOS-chem, *Science of The Total Environment*, 876, 162825, <https://doi.org/10.1016/j.scitotenv.2023.162825>, 2023.

Teets, A., Moore, D., Alexander, M., Blanken, P., Bohrer, G., Burns, S., Carbone, M., Ducey, M., Fraver, S., Gough, C., Hollinger, D., Koch, G., Kolb, T., Munger, J., Novick, K., Ollinger, S., Ouimette, A., Pederson, N., Ricciuto, D., and Richardson, A.: Coupling of tree growth and photosynthetic carbon uptake across six North American forests, *Journal of Geophysical Research: Biogeosciences*, 127, e2021JG006690, <https://doi.org/10.1029/2021JG006690>, 2022.

Touma, D., Stevenson, S., Lehner, F., and Coats, S.: Human-driven greenhouse gas and aerosol emissions cause distinct regional impacts on extreme fire weather, *Nature Communications*, 12, 212, <https://doi.org/10.1038/s41467-020-20570-w>, 2021.

Tyukavina, A., Potapov, P., Hansen, M. C., Pickens, A. H., Stehman, S. V., Turubanova, S., Parker, D., Zalles, V., Lima, A., Kommareddy, I., Song, X.-P., Wang, L., and Harris, N.: Global trends of forest loss due to fire from 2001 to 2019, *Frontiers in Remote Sensing*, 3, 825190, <https://doi.org/10.3389/frsen.2022.825190>, 2022.

van der Velde, I. R., van der Werf, G. R., Houweling, S., Eskes, H. J., Veefkind, J. P., Borsdorff, T., and Aben, I.: Biomass burning combustion efficiency observed from space using measurements of CO and NO₂ by the TROPOspheric monitoring instrument (TROPOMI), *Atmospheric Chemistry and Physics*, 21, 597–616, <https://doi.org/10.5194/acp-21-597-2021>, 2021.

van der Werf, G. R., Morton, D. C., DeFries, R. S., Giglio, L., Randerson, J. T., Collatz, G. J., and Kasibhatla, P. S.: Estimates of fire emissions from an active deforestation region in the southern amazon based on satellite data and biogeochemical modelling, *Biogeosciences*, 6, 235–249, <https://doi.org/10.5194/bg-6-235-2009>, 2009.

Vadrevu, K. and Lasko, K.: Intercomparison of MODIS AQUA and VIIRS I-band fires and emissions in an agricultural landscape — implications for air pollution research, *Remote Sensing*, 10, 978, <https://doi.org/10.3390/rs10070978>, 2018.

van der Werf, G. R., Randerson, J. T., Giglio, L., Collatz, G. J., Kasibhatla, P. S., and Arellano, A. F. J.: Interannual variability in global biomass burning emissions from 1997 to 2004, *Atmospheric Chemistry and Physics*, 6, 3423–3441, <https://doi.org/10.5194/acp-6-3423-2006>, 2006.

van der Werf, G. R., Randerson, J. T., Giglio, L., van Leeuwen, T. T., Chen, Y., Rogers, B. M., Mu, M., van Marle, M. J. E., Morton, D. C., Collatz, G. J., Yokelson, R. J., and Kasibhatla, P. S.: Global fire emissions estimates during 1997–2016, *Earth System Science Data*, 9, 697–720, <https://doi.org/10.5194/essd-9-697-2017>, 2017.

van Leeuwen, T. T., Peters, W., Krol, M. C., and van der Werf, G. R.: Dynamic biomass burning emission factors and their impact on atmospheric CO mixing ratios, *Journal of Geophysical Research: Atmospheres*, 118, 6797–6815, <https://doi.org/10.1002/jgrd.50478>, 2013.

van Wees, D., van der Werf, G. R., Randerson, J. T., Andela, N., Chen, Y., and Morton, D. C.: The role of fire in global forest loss dynamics, *Global Change Biology*, 27, 2377–2391, <https://doi.org/10.1111/gcb.15591>, 2021.

Vermote, E., Ellicott, E., Dubovik, O., Lapyonok, T., Chin, M., Giglio, L., and Roberts, G. J.: An approach to estimate global biomass burning emissions of organic and black carbon from MODIS fire radiative power, *Journal of Geophysical Research: Atmospheres*, 114, D18205, <https://doi.org/10.1029/2008JD011188>, 2009.

Vernooij, R., Eames, T., Russell-Smith, J., Yates, C., Beatty, R., Evans, J., Edwards, A., Ribeiro, N., Wooster, M., Strydom, T., Giongo, M. V., Borges, M. A., Menezes Costa, M., Barradas, A. C. S., van Wees, D., and Van der Werf, G. R.: Dynamic savanna burning emission factors based on satellite data using a machine learning approach, *Earth System Dynamics*, 14, 1039–1064, <https://doi.org/10.5194/esd-14-1039-2023>, 2023.

Wang, F., Harindintwali, J. D., Wei, K., Shan, Y., Mi, Z., Costello, M. J., Grunwald, S., Feng, Z., Wang, F., Guo, Y., Wu, X., Kumar, P., Kästner, M., Feng, X., Kang, S., Liu, Z., Fu, Y., Zhao, W., Ouyang, C., Shen, J., Wang, H., Chang, S. X., Evans, D. L., Wang, R., Zhu, C., Xiang, L., Rinklebe, J., Du, M., Huang, L., Bai, Z., Li, S., Lal, R., Elsner, M., Wigneron, J.-P., Florindo, F., Jiang, X., Shaheen, S. M., Zhong, X., Bol, R., Vasques, G. M., Li, X., Pfautsch, S., Wang, M., He, X., Agathokleous, E., Du, H., Yan, H., Kengara, F. O., Brahushi, F., Long, X.-E., Pereira, P., Ok, Y. S., Rillig, M. C., Jeppesen, E., Barceló, D., Yan, X., Jiao, N., Han, B., Schäffer, A., Chen, J. M., Zhu, Y., Cheng, H., Amelung, W., Spötl, C., Zhu, J., and Tiedje, J. M.: Climate change: strategies for mitigation and adaptation, *The Innovation Geoscience*, 1, 100015, [doi:10.59717/j.xinn-geo.2023.100015](https://doi.org/10.59717/j.xinn-geo.2023.100015), 2023.

Whitburn, S., Damme, M. V., Clarisse, L., Turquety, S., Clerbaux, C., and Coheur, P.-F.: Doubling of annual ammonia emissions from the peat fires in Indonesia during the 2015 El Niño, *Geophysical Research Letters*, 43, 11007–11014, <https://doi.org/10.1002/2016GL070620>, 2016.

Whittaker, R. H. and Likens, G. E.: Carbon in the biota, in: *Carbon and the Biosphere*, edited by: Woodwell, G. M. and Pecan, E. V., U.S. Atomic Energy Commission, Washington, D.C., 281–302, 1972.

Wiedinmyer, C., Kimura, Y., McDonald-Buller, E. C., Emmons, L. K., Buchholz, R. R., Tang, W., Seto, K., Joseph, M. B., Barsanti, K. C., Carlton, A. G., and Yokelson, R.: The fire inventory from NCAR version 2.5: An updated global fire emissions model for climate and chemistry applications, *Geoscientific Model Development*, 16, 3873–3891, <https://doi.org/10.5194/gmd-16-3873-2023>, 2023.

Wiedinmyer, C., Quayle, B., Geron, C., Belote, A., McKenzie, D., Zhang, X., O'Neill, S., and Wynne, K. K.: Estimating emissions from fires in North America for air quality modeling, *Atmospheric Environment*, 40, 3419–3432, <https://doi.org/10.1016/j.atmosenv.2006.02.010>, 2006.

Wiggins, E. B., Andrews, A., Sweeney, C., Miller, J. B., Miller, C. E., Veraverbeke, S., Commane, R., Wofsy, S., Henderson, J. M., and Randerson, J. T.: Boreal forest fire CO and CH₄ emission factors derived from tower observations in Alaska during the extreme fire season of 2015, *Atmospheric Chemistry and Physics*, 21, 8557–8574, <https://doi.org/10.5194/acp-21-8557-2021>, 2021.

Wiggins, E. B., Czimczik, C. I., Santos, G. M., Chen, Y., Xu, X., Holden, S. R., Randerson, J. T., Harvey, C. F., Kai, F. M., and Yu, L. E.: Smoke radiocarbon measurements from Indonesian fires provide evidence for burning of millennia-aged peat, *Proceedings of the National Academy of Sciences*, 115, 12419–12424, <https://doi.org/10.1073/pnas.1806003115>, 2018.

Williams, J. E., Weele, M. van, Velthoven, P. F. J. van, Scheele, M. P., Liousse, C., and Werf, G. R. van der: The impact of uncertainties in African biomass burning emission estimates on modeling global air quality, long range transport and tropospheric chemical lifetimes, *Atmosphere*, 3, 132–163, <https://doi.org/10.3390/atmos3010132>, 2012.

Wooster, M. J., Roberts, G., Perry, G. L. W., and Kaufman, Y. J.: Retrieval of biomass combustion rates and totals from fire radiative power observations: FRP derivation and calibration relationships between biomass consumption and fire radiative energy release, *Journal of Geophysical Research: Atmospheres*, 110, D24310, <https://doi.org/10.1029/2005JD006318>, 2005.

Yin, S.: Decadal trends of MERRA-estimated PM_{2.5} concentrations in East Asia and potential exposure from 1990 to 2019, *Atmospheric Environment*, 264, 118690, doi:10.1016/j.atmosenv.2021.118690, 2021.

Yin, S., Shi, C., Letu, H., Ito, A., Shang, H., Ji, D., Li, L., Bilige, S., Nie, T., Yi, K., Guo, M., Sun, Z., and Li, A.: Reconstruction of PM_{2.5} concentrations in east asia on the basis of a wide-deep ensemble machine learning framework and estimation of the potential exposure level from 1981 to 2020, *Engineering*, 49, 225–237, <https://doi.org/10.1016/j.eng.2024.09.025>, 2025.

Yin, S., Wang, X., Guo, M., Santoso, H., and Guan, H.: The abnormal change of air quality and air pollutants induced by the forest fire in sumatra and borneo in 2015, *Atmospheric Research*, 243, 105027, <https://doi.org/10.1016/j.atmosres.2020.105027>, 2020a.

Yin, S.: Effect of biomass burning on premature mortality associated with long-term exposure to PM_{2.5} in Equatorial Asia, *Journal of Environmental Management*, 330, 117154, <https://doi.org/10.1016/j.jenvman.2022.117154>, 2023.

Yin, S.: Exploring the relationships between ground-measured particulate matter and satellite-retrieved aerosol parameters in China, *Environmental Science and Pollution Research*, 29, 44348–44363, doi:10.1007/s11356-022-19049-6, 2022.

Yin, Y., Bloom, A. A., Worden, J., Saatchi, S., Yang, Y., Williams, M., Liu, J., Jiang, Z., Worden, H., Bowman, K., Frankenberg, C., and Schimel, D.: Fire decline in dry tropical ecosystems enhances decadal land carbon sink, *Nature Communications*, 11, 1900, <https://doi.org/10.1038/s41467-020-15852-2>, 2020b.

Zhang, F., Wang, J., Ichoku, C., Hyer, E. J., Yang, Z., Ge, C., Su, S., Zhang, X., Kondragunta, S., and Kaiser, J. W.: Sensitivity of mesoscale modeling of smoke direct radiative effect to the emission inventory: A case study in northern sub-saharan african region, *Environmental Research Letters*, 9, 075002, <https://doi.org/10.1088/1748-9326/9/7/075002>, 2014.

Zhang, Y., Albinet, A., Petit, J.-E., Jacob, V., Chevrier, F., Gille, G., Pontet, S., Chrétien, E., Dominik-Sègue, M., Levigoureux, G., Močnik, G., Gros, V., Jaffrezo, J.-L., and Favez, O.: Substantial brown carbon emissions from wintertime residential wood burning over france, *Science of The Total Environment*, 743, 140752, <https://doi.org/10.1016/j.scitotenv.2020.140752>, 2020.

Zheng, B., Ciais, P., Chevallier, F., Chuvieco, E., Chen, Y., and Yang, H.: Increasing forest fire emissions despite the decline in global burned area, *Science Advances*, 7, eabh2646, <https://doi.org/10.1126/sciadv.abh2646>, 2021.

Zheng, B., Ciais, P., Chevallier, F., Yang, H., Canadell, J. G., Chen, Y., van der Velde, I. R., Aben, I., Chuvieco, E., Davis, S. J., Deeter, M., Hong, C., Kong, Y., Li, H., Li, H., Lin, X., He, K., and Zhang, Q.:

Record-high CO₂ emissions from boreal fires in 2021, *Science*, 379, 912–917,
<https://doi.org/10.1126/science.ade0805>, 2023.